Springer Handbook

# of Atomic, Molecular, and Optical Physics

Gordon W. F. Drake (Ed.)

With CD-ROM, 288 Figures and 111 Tables

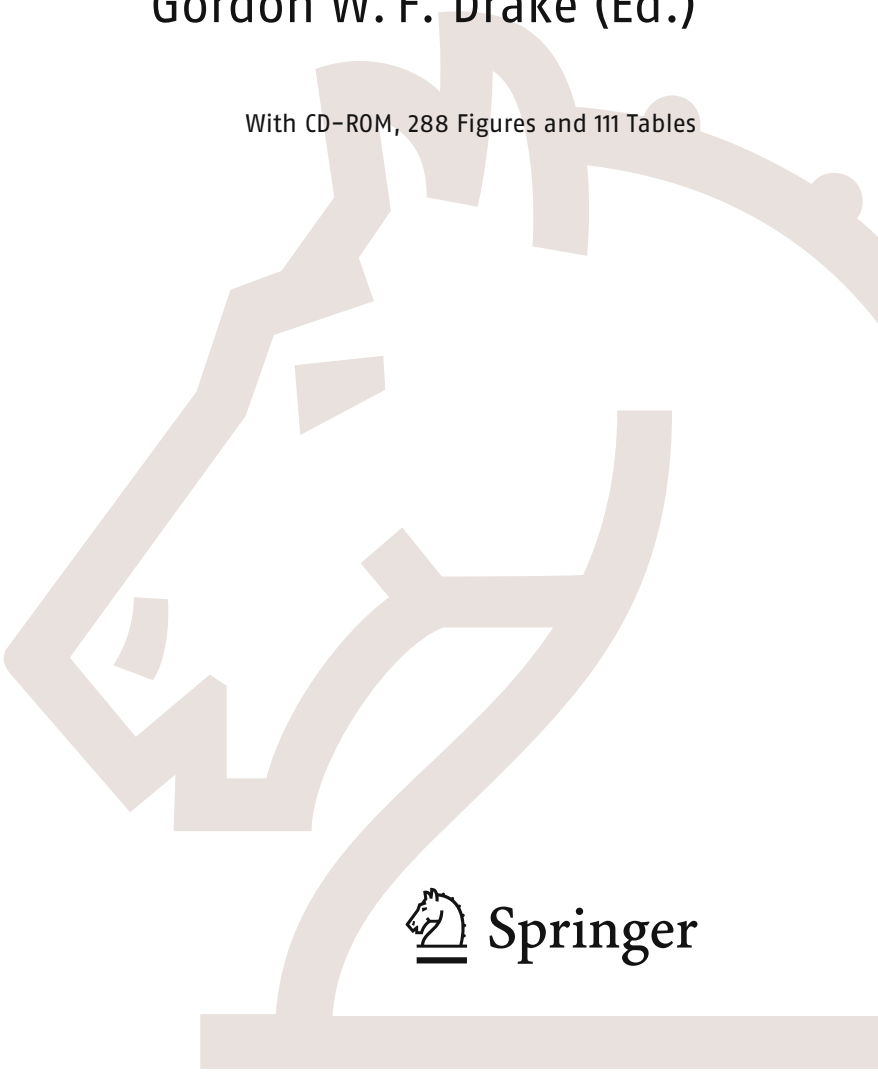

Springer

Springer Handbooks
of Atomic, Molecular, and Optical Physics

32. Molecular Symmetry and Dynamics

Molecules are aggregates of two or more nuclei bound by at least one electron. The nuclei of most stable molecules can be imagined to be points in a more or less rigid body whose relative positions are constrained by an electronic bonding potential. This potential depends strongly upon the electronic state as described in Chapt. 31. Most of this discussion is about stable molecules in their electronic ground state. In Sect. 32.6 some comments are made about molecules with excited, or "loose", parts.

32.1 Dynamics and Spectra of Molecular Rotors

Motions that stretch or compress the bonds are called vibrational motions, and give rise to spectral resonances in the infrared region of the spectrum. Typical fundamental vibrational quanta (ν_0) lie between $80\,\mathrm{cm}^{-1}$ (the lowest $GeBr_4$ mode) and $3020\,\mathrm{cm}^{-1}$ (the highest CH_4 mode). (A $1000\,\mathrm{cm}^{-1}$ wave has a wavelength of $10\,\mu\mathrm{m}$ and a frequency defined by the speed of light: 29.979 2458 THz.) Vibrational amplitudes are usually tiny since zero-point motions or vibrations involving one or two quanta ($\nu = 0, 1, 2, \ldots$) are constrained by the steep bonding potential to less than a few percent of the bond lengths, but high overtones may lead to dissociation, i. e., molecular breakup.

Overall rotation of molecules in free space is unconstrained, and gives rise to far-infrared or microwave pure rotational transitions or sidebands on top of vibrational spectra. Typical rotational quanta ($2B$) lie between $0.18\,\mathrm{cm}^{-1}$ (5.4 GHz) for SF_6 and $10.6\,\mathrm{cm}^{-1}$ for CH_4. Individual molecules are free to rotate or translate as a whole while undergoing tiny but usually rapid vibrations. Vibrating molecules may be thought of as tumbling collections of masses held together by 'springs' (the electronic vibrational potential or force field), and are called semirigid rotors. The coupling of rotational and vibrational motion is called rovibrational coupling and includes centrifugal and Coriolis coupling, which will be introduced in Sect. 32.6.

This discussion of molecular dynamics and spectra mainly involves molecular rotation and properties of rotationally excited molecules, particularly those with high rotational quantum number $J = 10–200$. However, the discussion also applies to molecules in excited vibrational states, and even certain cases of molecules in excited electronic states. The analysis of vibronic (vibrational-electronic), rovibrational (rotation–vibration), or rovibronic (all three) types of excitation can be very complicated [32.1–5] and is beyond the scope of this article, but these problems can all benefit from the elementary considerations described here.

32.1.1 Rigid Rotors

As a first approximation, and for the purposes of discussing basic molecular dynamics and spectra, one may ignore vibrations and model stable molecules as 'stick-and-ball' structures or rigid rotors. Then the Hamiltonian has just three terms:

$$H = AJ_x^2 + BJ_y^2 + CJ_z^2 \,. \tag{32.1}$$

Here $\{J_x, J_y, J_z\}$ are rotational angular momentum operators, and the rotational constants are half the inverses of the principal moments of inertia I_α of the body:

$$A = \frac{1}{2I_x} \,, \quad B = \frac{1}{2I_y} \,, \quad C = \frac{1}{2I_z} \,. \tag{32.2}$$

This implies that the J-coordinate system being used is a special one fixed to the rotor's body and aligned to its principal axes, an elementary body, or Eckart, frame.

Many molecules, particularly all diatomic molecules, have two of these rotational constants equal, say, $A = B$. Such rotors are called symmetric tops, and their Hamiltonian can be written in terms of the square of the total angular momentum $\boldsymbol{J} \cdot \boldsymbol{J}$ and one other body component J_z as

$$\begin{aligned} H &= BJ_x^2 + BJ_y^2 + CJ_z^2 \\ &= BJ_x^2 + BJ_y^2 + BJ_z^2 + (C-B)J_z^2 \\ &= B\boldsymbol{J}\cdot\boldsymbol{J} + (C-B)J_z^2 \end{aligned} \tag{32.3}$$

This gives a simple formula for the symmetric top rotational energy levels in terms of the quantum numbers J for the total angular momentum and K for the body z-component:

$$E(J,K) = BJ(J+1) + (C-B)K^2 \tag{32.4}$$

However, this eigenvalue formula may be a little too simple, since it hides the structure of the eigenstates or eigenfunctions. Indeed, the full Schrödinger angular differential equation based upon the Hamiltonian (32.1) is more lengthy. One should remember that H is written in a rotating body coordinate frame that must be connected to a star-fixed, or laboratory, frame in order to get the full theory.

32.1.2 Molecular States Inside and Out

Rotor angular momentum eigenfunctions can be expressed as continuous linear combinations of rotor angular position states $|\alpha\beta\gamma\rangle$ defined by Euler angles of the lab azimuth α, the polar angle β of body z-axis, and the body azimuth, or 'gauge twist', γ. The eigenfunctions are,

$$\left| \begin{matrix} J \\ MK \end{matrix} \right\rangle = \frac{\sqrt{2J+1}}{8\pi^2} \int_0^{2\pi} \mathrm{d}\alpha \int_0^{\pi} \sin\beta \, \mathrm{d}\beta \times \int_0^{2\pi} \mathrm{d}\gamma \, {D^J_{MK}}^*(\alpha\beta\gamma) |\alpha\beta\gamma\rangle \,, \tag{32.5}$$

where the rotor wave functions ${D^J_{MK}}^*$ are just the conjugates of the Wigner rotation matrices described in Sect. 32.3.1, and row and column indices M and K, respectively, are the lab and body components of the angular momentum [32.5–7].

An important feature of polyatomic molecules is that their angular momentum states have two kinds of azimuthal quantum numbers. In addition to the usual lab component of momentum M associated with the lab coordinate α (α and β are usually labeled φ and ϑ), there is a body component K associated with the Euler coordinate γ, the body azimuthal angle of the laboratory Z-axis relative to the body z-axis.

The physics of atomic or diatomic angular momentum states has no internal or "body" structure, so the quantum number K is always zero. Unless one sets $K = 0$, the energy formula (32.4) blows up for a point particle because z-inertia for a point is zero and C is infinite. Also, the dimension of the angular momentum state multiplet of a given J is larger than the usual $(2J+1)$ found in atomic or diatomic molecular physics. In polyatomic rotors, the number of states for each J is $(2J+1)^2$, since both quantum numbers M and K range between -J and +J.

A further important feature is that the molecular rotor wave functions contain, as a special ($K = 0$) case, all

the usual atomic spherical harmonics Y_m^ℓ complete with correct normalization and phase, since

$$\sqrt{4\pi}\,Y_m^\ell(\varphi\vartheta) = D_{m0}^\ell(\varphi\vartheta\cdot)^*\sqrt{2\ell+1}\,. \tag{32.6}$$

This is part of a powerful symmetry principle: group representations are quantum wave functions, and symmetry analysis is an extension of Fourier analysis – not just for translations as in Fourier's original work, but for any group of symmetry operations. The usual Fourier coefficients e^{ikx} are replaced by the D functions in the rotational Fourier transform embodied by (32.5).

Molecular rotational analysis displays another important but little known aspect of symmetry analysis in general. For every group of symmetry operations, such as the external lab-based rotations familiar to atomic physics, there is an independent dual group of internal or body-based operations. The external symmetry of the environment or laboratory is independent of the internal symmetry of the molecular body, and all the operations of one commute with all those of the other. The molecular rotation group is thus written as an outer product $R(3)_{\text{LAB}} \otimes R(3)_{\text{BODY}}$ of the external and internal parts, and the degeneracy associated with this group's representations for a single J is $(2J+1)^2$ as mentioned above. It is a special $\otimes$-product, however, since the J-number is shared.

The inversion or parity operator $\boldsymbol{I}(\boldsymbol{r} \to -\boldsymbol{r})$ can be defined to be the same for both lab and body frames. Including $\boldsymbol{I}$ with the rotational group $R(3)$ gives the orthogonal group $O(3) = R(3) \otimes \{\boldsymbol{I}, \boldsymbol{I}\}$. If parity is conserved (e.g., no weak neutral currents), the fundamental molecular orthogonal group is $O(3)_{\text{LAB}} \otimes O(3)_{\text{BODY}}$.

How this symmetry breaks down and which levels split depends upon both the perturbative laboratory environment and the internal molecular structure. A spherical top Hamiltonian is (32.1) with $A = B = C$. This has a full $O(3)_{\text{BODY}}$ (spherical) symmetry since it is just $B\boldsymbol{J}\cdot\boldsymbol{J}$. Given that the rotor is in an $O(3)_{\text{LAB}}$ laboratory (empty space), the original symmetry $O(3)_{\text{LAB}} \otimes O(3)_{\text{BODY}}$ remains intact and the $(2J+1)^2$ degeneracy is to be expected. However, a symmetric rotor in a lab vacuum has its internal symmetry broken down to $O(2)_{\text{BODY}}$ if $A = B \neq C$, and the energies given by (32.4) consist of internal quantum singlets for $K = 0$ and $\pm K$ doublets for $K \neq 0$. But each of these levels still has a lab degeneracy of $(2J+1)$ if $O(3)_{\text{LAB}}$ is still in effect. So the $(2J+1)^2$ level degeneracies are each split into multiplets of degeneracy $(2J+1)$ and $2(2J+1)$ for $K = 0$ and $K \neq 0$, respectively. The resulting levels are often labeled $\Sigma, \Pi, \Delta, \Phi, \Gamma, \ldots$ in a somewhat inappropriate analogy with the atomic s, p, d, f, g, ... labels of Bohr model electronic orbitals.

Only by perturbing the lab environment can one reduce the $O(3)_{\text{LAB}}$ symmetry and split the M degeneracies. For example, a uniform electric field would reduce the $O(3)_{\text{LAB}}$ to an $O(2)_{\text{LAB}}$, giving Stark splittings which consist of external quantum singlets for $M = 0$ and $\pm M$ doublets for $M \neq 0$. A uniform magnetic field would reduce the $O(3)_{\text{LAB}}$ to an $R(2)_{\text{LAB}}$, giving Zeeman splittings into external quantum singlets for each M. The analogy between atomic external field splitting and internal molecular rotational structure splitting is sometimes a useful one and will be used later.

32.1.3 Rigid Asymmetric Rotor Eigensolutions and Dynamics

The general case for the rigid rotor Hamiltonian (32.1) has three unequal principal moments of inertia ($A \neq B \neq C$). This is called the rigid asymmetric top Hamiltonian, and provides a first approximation for modeling rotation of low symmetry molecules, such as H_20. Also, a number of properties of its eigensolutions are shared by more complicated systems. The dynamics of an asymmetric top is quite remarkable, as demonstrated by tossing a tennis racquet in the air, flat side up. The corresponding quantum behavior of such a molecule is also nontrivial.

Given the total angular momentum J, one may construct a $(2J+1)$-dimensional matrix representation of H using standard matrix elements of the angular momentum operators J_x, J_y, and J_z, as given in Chapt. 2. The H matrix connects states with $(2J+1)$-different body quantum numbers $K(-J \leq K \leq J)$, but the matrix is independent of the lab quantum numbers M, so there are $(2J+1)$ identical H matrices; one for each value of the lab quantum number $M(-J \leq K \leq J)$.

A plot of the 21 eigenvalues of (32.1) for $J = 10$ is shown in Fig. 32.1. Here, the constants are set to $A = 0.2\,\text{cm}^{-1}$ and $C = 0.6\,\text{cm}^{-1}$, while B is varied between $B = A$, which corresponds to a prolate symmetric top (an elongated cylindrical object) and $B = C$, which corresponds to an oblate symmetric top (a flattened cylindrical object or discus). For all B values between those of A and C, the object is asymmetric.

The left hand end $\left(A = B = 0.2\,\text{cm}^{-1},\ C = 0.6\,\text{cm}^{-1}\right)$ of the plot in Fig. 32.1 corresponds to a prolate symmetric top. The symmetric top level spectrum is given by (32.4). It consists of a lowest singlet state corresponding to $K = 0$ and an ascending quadratic ladder of doublets corresponding to $K = \pm 1, \pm 2, \ldots, \pm J$.

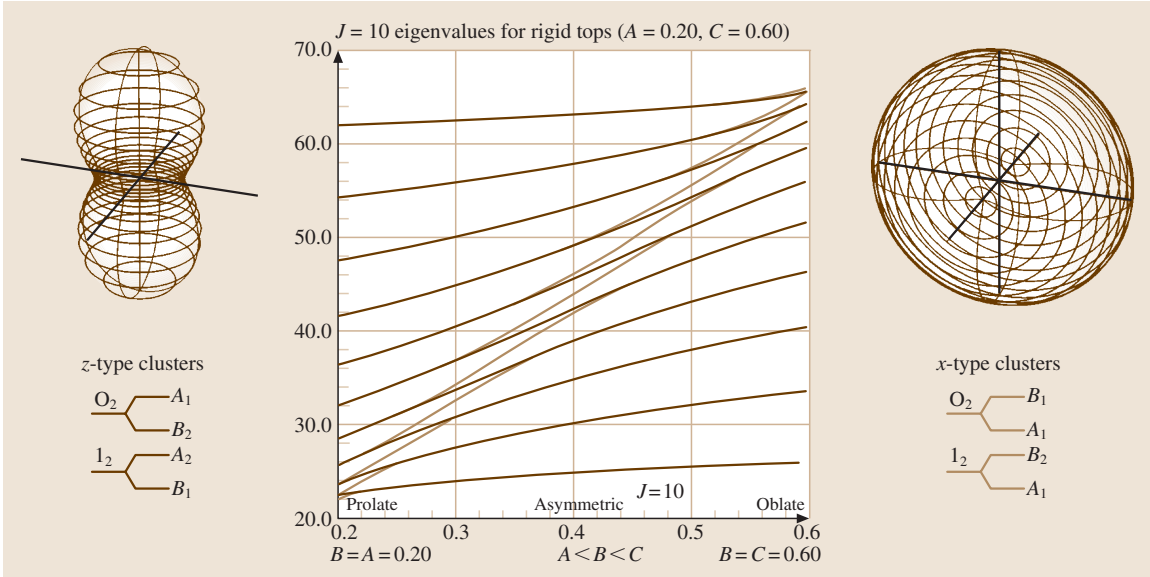

Fig. 32.1 $J = 10$ eigenvalue plot for symmetric rigid rotors. ($A = 0.2$, $C = 0.6\,\mathrm{cm}^{-1}$ $A < B < C$). Prolate and oblate RE surfaces are shown

The right hand end $\left(A = 0.2\,\mathrm{cm}^{-1}, B = C = 0.6\,\mathrm{cm}^{-1}\right)$ of the plot corresponds to an oblate symmetric top with a descending quadratic ladder of levels, the $K = 0$ level being highest. Also, the internal K-axis of quantization switches from the body z-axis for $\left(A = B = 0.2\,\mathrm{cm}^{-1}, C = 0.6\,\mathrm{cm}^{-1}\right)$ to the body x-axis for $\left(A = 0.2\,\mathrm{cm}^{-1}, B = C = 0.6\,\mathrm{cm}^{-1}\right)$. Note that the lab M-degeneracy is invisible here, but exists nevertheless.

For intermediate values of B, one has an asymmetric top level structure and, strictly speaking, no single axis of quantization. As a result, the eigenlevel spectrum is quite different. A detailed display of asymmetric top levels for the case $\left(A = 0.2\,\mathrm{cm}^{-1}, B = 0.4\,\mathrm{cm}^{-1}, C = 0.6\,\mathrm{cm}^{-1}\right)$ is given at the bottom of Fig. 32.2. They are shown to correspond to semiclassical orbits discussed in Sect. 32.2. This example is the most asymmetric top, since parameter B has a value midway between the symmetric top limits of $B = A$ and $B = C$.

The twenty-one $J = 10$ asymmetric top levels are arranged into roughly ten asymmetry doublets and one singlet. This resembles the symmetric top levels except that doublets are split by varying amounts, and the singlet is isolated from the other levels in the middle of the band instead of being crowded at the top or bottom. The doublet splittings are magnified in circles drawn next to the levels, and these indicate that the splitting decreases quasi-exponentially with each doublet's separation from the central singlet.

An asymmetric doublet splitting is also called superfine structure and can be viewed as the result of a dynamic tunneling process in a semiclassical model of rotation [32.8–10]. Such a model clarifies the classical-quantum correspondence for polyatomic rovibrational dynamics in general. It can also help to derive simple approximations for eigenvalues and eigenvectors.

32.2 Rotational Energy Surfaces and Semiclassical Rotational Dynamics

A semiclassical model of molecular rotation can be based upon what is called a rotational energy surface (RES) [32.7–14]. Examples of RES for an asymmetric top are shown in Fig. 32.2, and for prolate and oblate symmetric tops in Fig. 32.1. Each surface is a radial plot of the classical energy derived from the Hamiltonian (32.1) as a function of the polar direction of the classical angular momentum $\boldsymbol{J}$-vector in the body frame. The magnitude of $\boldsymbol{J}$ is fixed for each surface. Note that the $\boldsymbol{J}$-vector in the lab frame is a classical constant of the motion if there are no external perturbations. However, $\boldsymbol{J}$ may gyrate considerably in the moving body frame,

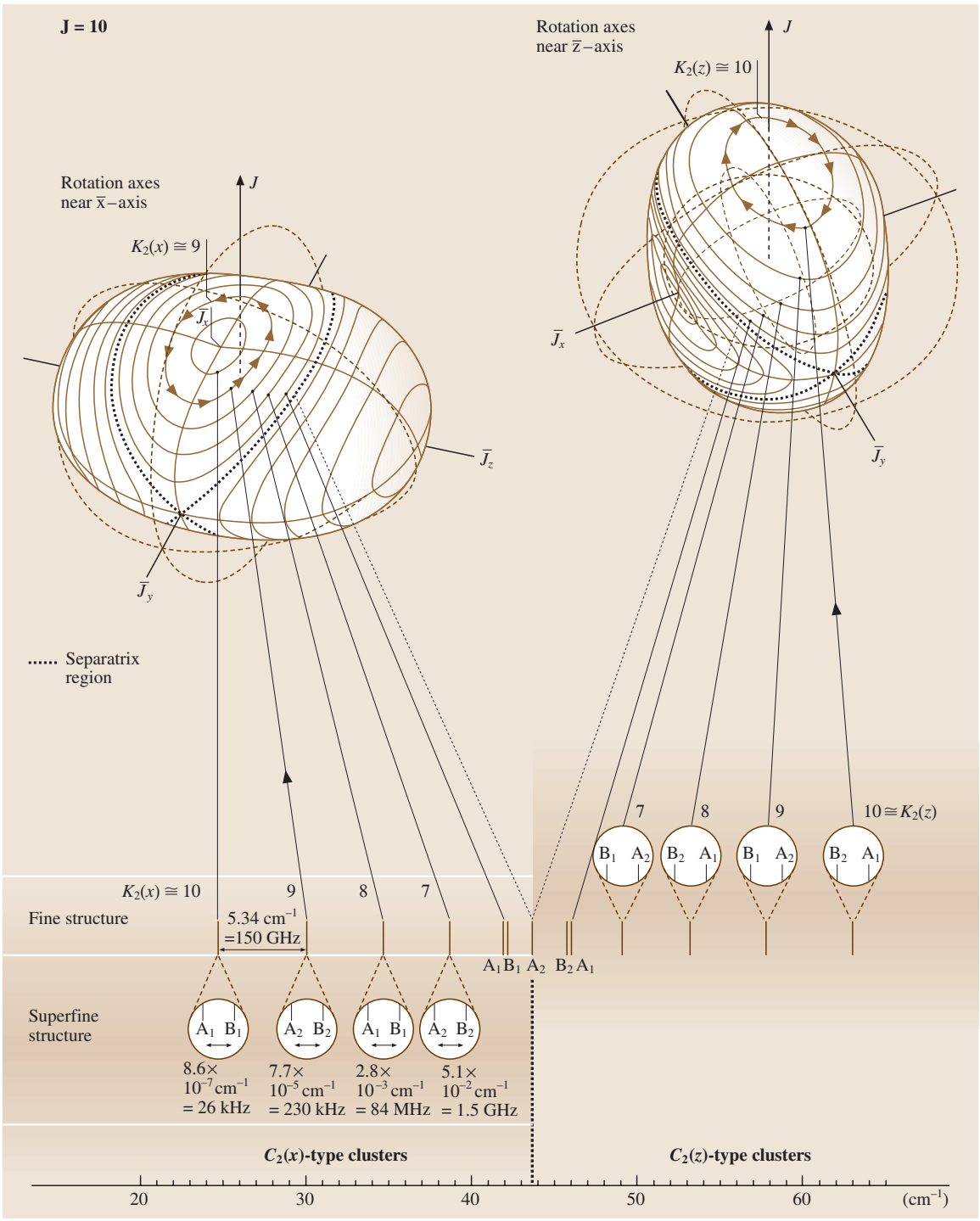

Fig. 32.2 $J = 10$ rotational energy surface and related level spectrum for an asymmetric rigid rotator $(A = 0.2,\ B = 0.4,\ C = 0.6\,\mathrm{cm}^{-1})$

but its magnitude $|\boldsymbol{J}|$ stays the same in all frames for free rotation.

An RES differs from what is called a constant energy surface (CES), which is obtained by simply plotting $E = H = \text{const.}$ in $\boldsymbol{J}$-space using (32.1). A rigid rotor CES is an ellipsoid covering a range of $|\boldsymbol{J}|$ values at a single energy. An RE surface, on the other hand, is a spherical harmonic plot at a single $|\boldsymbol{J}|$ value for a range of energies. The latter is more appropriate for spectroscopic studies of fine structure, since one value of the rotational quantum number J corresponds to a multiplet of energy levels or transitions. An RES also shows loci of high and low energy rotations. Also, it has roughly the same shape as the body it represents, i. e., an RES is long in the direction that the corresponding molecule is long (but vice-versa for CES).

For a freely rotating molecule, the laboratory components of the classical total angular momentum $\boldsymbol{J}$ are constant. If one chooses to let $\boldsymbol{J}$ define the lab Z-axis, then the direction of the $\boldsymbol{J}$-vector in the body frame is given by polar and body azimuthal coordinates β and γ, which are the second and third Euler angles, respectively. (It is conventional to use the negatives $-\beta$ and $-\gamma$ as polar coordinates, but this will not be necessary here.) Then the body components of the $\boldsymbol{J}$-vector are written as

$$\begin{aligned}&\left(J_x = |J| \sin\beta\cos\gamma\,, \quad J_y = |J| \sin\beta\sin\gamma\,,\right.\\ &\left.J_z = |J| \cos\beta\right)\,,\end{aligned} \tag{32.7}$$

where the magnitude of the quantum value $|J| = \sqrt{J(J+1)} \cong J + \frac{1}{2}$.

Substituting this into the Hamiltonian (32.1) gives an expression for the general rigid rotor RES radius in polar coordinates:

$$\begin{aligned}E(\beta,\gamma) = \langle H\rangle &= J(J+1)\\ &\times\left[\sin^2\beta\left(A\cos^2\gamma + B\sin^2\gamma\right) + C\cos^2\beta\right]\,.\end{aligned} \tag{32.8}$$

The prolate symmetric top ($A = B < C$) expression

$$E(\beta) = \langle H\rangle = J(J+1)\left[B + (C-B)\cos^2\beta\right] \tag{32.9}$$

is independent of azimuthal angle γ. The 3-dimensional plots of these expressions are shown in Figs. 32.1 and 32.2.

The RES have topography lines of constant energy ($E = \text{const.}$) that are the intersection of an RES (constant $|\boldsymbol{J}|$) with spheres of constant energy. The topography lines are allowed classical paths of the angular momentum $\boldsymbol{J}$-vector in the body frame, since these paths conserve both energy and momentum.

The trajectories in these figures are special ones. They are the quantizing trajectories for total angular momentum $J = 10$. For the prolate symmetric top, the quantizing trajectories have integral values for the body z-component K of angular momentum. According to the Dirac vector model, angular momentum vectors trace out a cone of altitude K and slant height $|J| = \sqrt{J(J+1)}$. The quantizing polar angles Θ_k^J are given by

$$\begin{aligned}\Theta_K^J &= \cos^{-1}\frac{K}{\sqrt{J(J+1)}}\\ &(K = J, J-1, \cdots, -J)\,.\end{aligned} \tag{32.10}$$

These are the latitude angles of the paths on the RES in Fig. 32.1 for $K = 10, 9, 8, \ldots, -10$. (For the oblate RES, the angles are relative to the x-axis.) If $\beta = \left(\Theta_K^J\right)$ is substituted into the symmetric top RES (32.9), the result is

$$E\left(\Theta_K^J\right) = J(J+1)B + (C-B)\,K^2\,, \tag{32.11}$$

which is precisely the symmetric top eigenvalue (32.4). The quantizing paths are circles lying at the intersections of the Dirac angular momentum cones and the RES. The angle $\left(\Theta_K^J\right)$ is a measure of the angular momentum uncertainty ΔJ_x or ΔJ_y transverse to the z-axis of quantization. Clearly, $K = \pm J$ states have minimum uncertainty.

For the asymmetric top, the classical paths that conserve both $|J|$ and E are one of two types. First, there are those pairs of equal-energy orbits that go around the hills on the plus or minus end of the body z-axis, which correspond to the $\pm K$ pairs of levels in the upper half of the level spectrum drawn in Fig. 32.2. Then there are the pairs of levels belonging to the equal-energy orbits in either of the two valleys surrounding the body x-axis, which are associated with the pairs of levels in the lower half of the level spectrum. Different eigensolutions occupy different geography.

The upper pairs of paths are seen to be distorted versions of the prolate top orbits seen on the left-hand side of Fig. 32.1, while the lower pairs are distorted versions of the oblate top orbits seen on the right-hand side of Fig. 32.1. The distortion makes J_z deviate from a constant K-value and corresponds to K-mixing in the quantum states. This also shows that more than one axis of quantization must be considered; the prolate-like paths are based on the z-axis, while the oblate-like paths belong to the body x-axis.

The two types of orbits, x and y, are separated by what is called a separatrix curve, which crosses the sad-

dle points on either side of the body y-axis. In the example shown in Fig. 32.2, the separatrix is associated with a single level which separates the upper and lower energy doublets. The doublets that are closer to the separatrix level are split more than those which are farther away. Apart from the splitting, the energy levels can be obtained by generalized Bohr quantization of the classical paths on the RES. The quantization condition is,

$$\int J_z \, \mathrm{d}\gamma = K \,, \tag{32.12a}$$

where

$$J_z = \sqrt{\frac{J(J+1)\big(C\cos^2\gamma + B\sin^2\gamma\big) - E}{\big(C\cos^2\gamma + B\sin^2\gamma\big) - A}} \tag{32.12b}$$

follows from (32.7) and (32.8). The resulting E_K-values are obtained by iteration.

The doublet, or superfine, splitting is a quantum effect which may be associated with tunneling between orbits that would have had equal energies E_K in the purely classical or semiclassical model. Approximate tunneling rates are obtained from integrals over the saddle point between each pair of equal-energy quantizing paths. The K-th rate, or amplitude, is,

$$S_K = \nu_K \, \mathrm{e}^{-P_K} \,, \tag{32.13}$$

where

$$P_K = \mathrm{i}\int_{\gamma-}^{\gamma+} \mathrm{d}\gamma \sqrt{\frac{J(J+1)\big(C\cos^2\gamma + B\sin^2\gamma\big) - E_K}{\big(C\cos^2\gamma + B\sin^2\gamma\big) - A}} \tag{32.14}$$

is the saddle path integral between the points of closest approach, $\gamma+$ and $\gamma-$, and ν_K is the classical precession frequency or quantum level spacing around energy level E_K. Since there are two tunneling paths, the amplitude S_K is doubled in a tunneling Hamiltoni an matrix for the K-th semiclassical doublet of z and $-z = \overline{z}$ paths:

$$\langle H \rangle_K = \begin{pmatrix} E_K & 2S_K \\ 2S_K & E_K \end{pmatrix} \begin{matrix} |z\rangle \\ |\overline{z}\rangle \end{matrix} \,. \tag{32.15}$$

The resulting tunneling energy eigensolutions are given in Table 32.1.

A- or B-states correspond to symmetric and antisymmetric combinations of waves localized on the two semiclassical paths. Rotational symmetry is considered in Sect. 32.3.

The total doublet splitting is $4S_K$, and decreases exponentially with the saddle path integral (32.14). The superfine A–B splittings in Fig. 32.2 are seen to range from several GHz near the separatrix down to only 26 kHz for the highest-K doublets at the band edges.

Meanwhile, the typical interdoublet level spacing or classical precessional frequency is about 150 GHz for the $J = 10$ levels shown in Fig. 32.2. This K-level spacing is called rotational fine structure splitting, and is also present in the symmetric top case. (The superfine splitting of the symmetric top doublets is exactly zero, since they have $O(2)_{BODY}$ symmetry if $A = B$ or $B = C$. In this case, all tunneling amplitudes cancel.)

The classical precession of $\boldsymbol{J}$ in the body frame follows a "left-hand rule" similar to what meteorologists use to determine Northern Hemisphere cyclonic rotation. A left "thumbs-down" or "low" has counterclockwise precession as does an oblate rotor valley, but a prolate RES "high" supports clockwise motion just like a weather "high".

Finally, consider the spacing between adjacent J-levels, which is called rotational structure, in a spectrum. This spacing is

$$E(J, K) - E(J-1, K) = 2BJ \,, \tag{32.16}$$

according to the symmetric top energy formulas (32.4). For the example just treated, $2BJ$ is about $10\,\mathrm{cm}^{-1}$ or 300 GHz. This corresponds to the actual rotation frequency of the body. It is the only kind of rotational dynamics or spectrum that is possible for a simple diatomic rotor. A diatomic molecule, however, can have internal electronic or nuclear spin rotation, which gives an additional fine structure as discussed later [32.1,6,15].

To summarize, polyatomic molecules can be expected to exhibit all three types of rotational motion and spectra (from faster to slower): rotational, precessional, and precessional tunneling. These are related to three kinds of spectral structure (from coarser to finer spectra): rotational structure, fine structure, and superfine structure, respectively. Again, this neglects internal rotational and spin effects, which can have abnormally strong rotational resonance coupling due to the superfine structure [32.9,16]. Examples of this are discussed at the end of this chapter.

Table 32.1 Tunneling energy eigensolutions

Eigenvectors	$\|z\rangle$	$\|\overline{z}\rangle$	Eigenvalues
$\|A\rangle$	1	1	$E^A(K) = E_K + 2S_K$
$\|B\rangle$	1	−1	$E^B(K) = E_K - 2S_K$

32.3 Symmetry of Molecular Rotors

Molecular rotational symmetry is most easily introduced using examples of rigid rotors. Molecular rotor structures may have more or less internal molecular symmetry, depending on how their nuclei are positioned relative to one another in the body frame. A molecule's rotational symmetry is described by one of the elementary rotational point symmetry groups. These are the n-fold axial cyclic groups C_n and polygonal dihedral groups $D_n (n = 1, 2, \dots)$, the tetrahedral group T, the cubic-octahedral group O, or the icosahedral group Y. All other point groups, such as C_{nv}, T_d, and O_h, are a combination of an elementary point group with the inversion operation $\boldsymbol{I}(\boldsymbol{r} \to -\boldsymbol{r})$. Each of these groups consist of operations which leave at least one point (origin) of a structure fixed while mapping identical atoms or nuclei into each other in such a way that the appearance of the structure is unchanged. The point groups are subgroups of the nuclear permutation groups [32.17].

In other words, molecular symmetry is based upon one of the most fundamental properties of atomic physics: the absolute identity of all atoms or, more precisely, nuclei of a given atomic number Z and mass number A. It is the identity of the so-called 'elementary' electronic and nucleonic constituent particles that underlies the symmetry.

The Pauli principle states that all half-integer spin particles are antisymmetrized with every other one of their kind in the universe. The Pauli–Fermi antisymmetrization principle and the related Bose–Einstein symmetrization principle determine much of molecular symmetry and dynamics, just as the Pauli exclusion principle is fundamental to electronic structure.

32.3.1 Asymmetric Rotor Symmetry Analysis

For an asymmetric rigid rotor, any rotation which interchanges $x-$, $y-$, or z-axes of the body cannot possibly be a symmetry, since all three axes are assumed to have different inertial constants. This restricts one to consider only 180° rotations about the body axes, and these are the elements of the rotor groups C_2 and D_2.

The two symmetry types for C_2 are even (denoted A or 0_2) and odd (denoted B or 1_2) with respect to a 180° rotation. For D_2, which is just $C_2 \otimes C_2$, the four symmetry types are even-even (denoted A_1), even-odd (denoted A_2), odd-even (denoted B_1), and odd-odd (denoted B_2) with respect to 180° rotations about the y- and x-axes, respectively. (The z-symmetry is determined by a product of the other two since $\boldsymbol{R}_z = \boldsymbol{R}_x\ \boldsymbol{R}_y$.) This is summarized in the character Tables 32.2 and 32.3.

C_2	1	R
A	1	1
B	1	−1

Table 32.2 Character table for symmetry group C_2

The RES for the rigid rotor shown in Fig. 32.2 is invariant under 180° rotations about each of the three body axes. Therefore, its Hamiltonian symmetry is D_2 and its quantum eigenlevels must correspond to one of the four types listed under D_2 in Table 32.3. The D_2 symmetry labels are called rotational (or in general rovibronic) species of the molecular state. The species label the symmetry of a quantum wave function associated with a pair of C_2 symmetric semiclassical paths.

The classical $\boldsymbol{J}$-paths come in D_2 symmetric pairs, but each individual classical $\boldsymbol{J}$-path on the rigid rotor RES has a C_2 symmetry which is a subgroup of D_2. Each path in the valley around the x-axis is invariant under just the 180° rotation around the x-axis. This is $C_2(x)$ symmetry. The other member of its pair that goes around the negative x-axis also has this local $C_2(x)$ symmetry. The combined pair of paths has the full D_2 symmetry but classical mechanics does not permit occupation of two separate paths. Multiple path occupation is a completely quantum effect.

Similarly, each individual $\boldsymbol{J}$-path on the hill around the z-axis is invariant under just the 180° rotation around the z-axis, so it has $C_2(z)$ symmetry as does the equivalent path around the negative z-axis. Only the separatrix has the full D_2 symmetry, since its pairs are linked up on the y-axis to form the boundary between the x and z paths. No $\boldsymbol{J}$-paths encircle the unstable y-axis since it is a saddle point.

Each classical $\boldsymbol{J}$-path near the x- or z-axis belongs to a particular K-value through the semiclassical quantization conditions (32.12). Depending upon whether the K-value is even (0_2) or odd (1_2), the corresponding K-doublet is correlated with a pair of D_2 species as shown in the columns of the correlation tables in Fig. 32.3. These three correlation tables give the axial

Table 32.3 Character table for symmetry group D_2

D_2	1	R_x	R_y	R_z
A_1	1	1	1	1
A_2	1	−1	1	−1
B_1	1	1	−1	−1
B_2	1	−1	−1	1

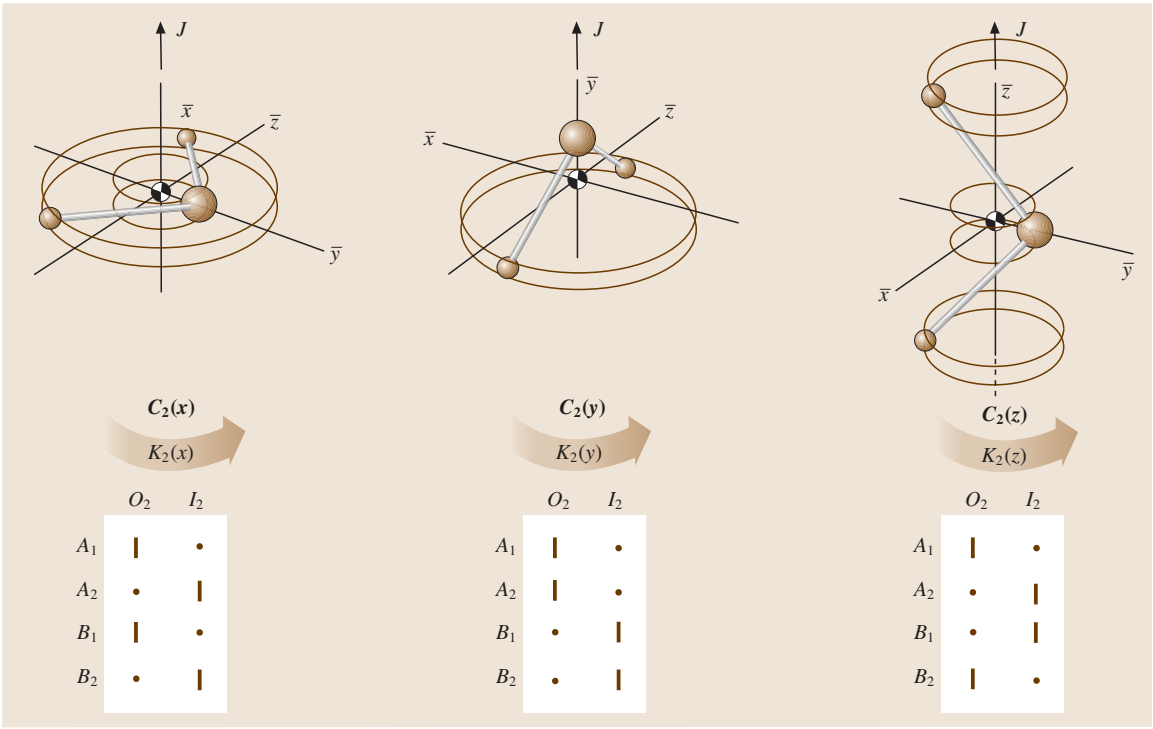

Fig. 32.3 Tables of correlations between D_2 symmetry species and the even (0_2) and odd (I_2) symmetric species of subgroups $C_2(x)$, $C_2(y)$, and $C_2(z)$

180° rotational symmetry of each D_2 species for rotation near each body axis x, y and z, respectively, but only the stable rotation axes x and z support stable path doublets for this Hamiltonian (32.1).

For example, consider the $K = 10$ paths which lie lowest in the x-axis valleys. Since $K = 10$ is even (0_2), it is correlated with an A_1 and B_1 superfine doublet [see the 0_2 column of the $C_2(x)$ table]. On the high end near the z-axis hilltop, $K = 10$ gives rise to an A_1 and B_2 doublet [see the 0_2 column of the $C_2(z)$ table]. All the doublets in Fig. 32.2 may be assigned in this way.

32.4 Tetrahedral–Octahedral Rotational Dynamics and Spectra

The highest symmetry rigid rotor is the *spherical top* for which the three inertial constants are equal ($A = B = C$). The spherical top Hamiltonian

$$H = B\boldsymbol{J}\cdot\boldsymbol{J}$$

has the full $R(3)_{\mathrm{LAB}} \otimes R(3)_{\mathrm{BODY}}$ symmetry. With inversion parity, the symmetry is $O(3)_{\mathrm{LAB}} \otimes O(3)_{\mathrm{BODY}}$. In any case, the J-levels are $(2J+1)^2$-fold degenerate. The resulting $BJ(J+1)$ energy expression is the first approximation for molecules which have regular polyhedral symmetry of, for example, a tetrahedron (CF_4), cube (C_6H_6), octahedron (SF_6), dodecahedron or icosahedron ($C_{20}H_{20}$, $B_{12}H_{12}$, or C_{60}). Rigid regular polyhedra have isotropic or equal inertial constants and rotate just like they were perfectly spherical distributions of mass.

However, no molecule can really have spherical $O(3)_{\mathrm{BODY}}$ symmetry; even molecules of the highest symmetry contain a finite number of nuclear mass points, and therefore have a finite internal point symmetry. Evidence of octahedral or tetrahedral symmetry shows up in fine structure splittings analogous to those for asymmetric tops. However, spherical top fine structure is due to symmetry breaking caused by anisotropic or tensor rotational distortion. To discuss this, one needs to consider what are called semirigid rotors.

32.4.1 Semirigid Octahedral Rotors and Centrifugal Tensor Hamiltonians

The lowest order tensor centrifugal distortion perturbation has the same form for both tetrahedral and octahedral molecules. It is simply a sum of fourth powers of angular momentum operators given in the third term below. The first two terms are the scalar rotor energy and scalar centrifugal energy.

$$H = B\,|J|^2 + D\,|J|^4 + 10t_{044} \times \left[J_x^4 + J_y^4 + J_z^4 - (3/5)J^4\right] . \qquad (32.17)$$

The tensor term includes the scalar $(3/5)J^4$ to preserve the center of gravity of the tensor level splitting. This type of semirigid rotor Hamiltonian was first used in the study of methane (CH_4) spectra [32.18].

The scalar terms do not reduce the symmetry or split the levels. The tensor term (t_{044}) breaks the molecular symmetry from $O(3)_{\mathrm{LAB}} \otimes O(3)_{\mathrm{BODY}}$ to the lower symmetry subgroup $O(3)_{\mathrm{LAB}} \otimes T_{d\mathrm{BODY}}$, or $O(3)_{\mathrm{LAB}} \otimes O_{h\mathrm{BODY}}$, and splits the $(2J+1)^2$-fold degeneracy into intricate fine structure patterns which are analogous to cubic crystal field splitting of atomic orbitals. The first calculations of the tensor spectrum were done by direct numerical diagonalization [32.18–21]. As a result, many of the subtle symmetry properties were missed. The semiclassical analysis [32.22] described in the following Sections exposes these properties.

32.4.2 Octahedral and Tetrahedral Rotational Energy Surfaces

By substituting in (32.7) and plotting the energy as a function of body polar angles β and γ, an RES is obtained, two views of which are shown in Fig. 32.4. Here the tensor term is exaggerated in order to exhibit the topography clearly. (In $(n = 0)$ SF_6, the t_{044} coefficient is only about 5.44 Hz, while the rotational constant is $B = 0.09\,\mathrm{cm}^{-1}$. The t_{244} coefficient of $(n = 1)$ SF_6 is much greater.)

A positive tensor coefficient ($t_{a44} > 0$) gives an octahedral shaped RES, as shown in Fig. 32.4. This is appropriate for octahedral molecules since they are least susceptible to distortion by rotations around the x-, y-, and z-axes containing the strong radial bonds. Thus the rotational energy is highest for a $\boldsymbol{J}$-vector near one of six body axes $(\pm1, 0, 0)$, $(0, \pm1, 0)$, or $(0, 0, \pm1)$, i. e., one of the six RES hills in Fig. 32.4.

However, if the $\boldsymbol{J}$-vector is set in any of the eight interaxial directions $(\pm1, \pm1, \pm1)$, the centrifugal force will more easily bend the weaker angular bonds, raise the molecular inertia, and lower the rotational energy. This accounts for the eight valleys on the RES in Fig. 32.4.

A negative tensor coefficient ($t_{a44} < 0$) gives a cubic shaped RES. This is usually appropriate for cubic and tetrahedral molecules, since they are most susceptible to distortion by rotations around the x-, y-, and z-axes which lie between the strong radial bonds on the cubic diagonals. Instead of six hills and eight valleys, one finds six valleys and eight hills on the cubic RES. Both freon CF_4 and cubane C_8H_8 are examples of this type of topology.

Note that a semirigid tetrahedral rotor may have the same form of rotational Hamiltonian and RE surface as a cubic rotor. The four tetrahedral atomic sites are in the same directions as four of the eight cubic sites. The other four cubic sites form an inverted tetrahedron of the same shape.

If only tetrahedral symmetry were required, the Hamiltonian could contain a third order tensor of the form $J_x J_y J_z$. However, pure rotational Hamiltonians must also satisfy time-reversal symmetry: the energy for each $\boldsymbol{J}$ must be the same as for $-\boldsymbol{J}$, and thus rotational sense should not matter. This symmetry excludes all odd powers of $\boldsymbol{J}$. Simple rotor RES have inversion symmetry even if their molecules do not. Compound rotors containing spins or other rotors may have "lopsided" pairs of RES as shown in Sect. 32.6.

32.4.3 Octahedral and Tetrahedral Rotational Fine Structure

An example of rotational fine structure for angular momentum quantum number $J = 30$ is shown in Fig. 32.4. The levels consist mainly of clusters of levels belonging to the octahedral symmetry species A_1, A_2, E, T_1, or T_2. The characters of these species are given in Table 32.4. (The tetrahedral T_d group has a similar table where T_1 and T_2 are often labeled F_1 and F_2).

The first column gives the dimension or degeneracy of each species; A_1, A_2, are singlets, E is a doublet,

Table 32.4 Character table for symmetry group O

O	0°	120°	180°	90°	180°
A_1	1	O 1	1	1	1
A_2	1	1	1	−1	−1
E	2	−1	2	0	0
T_1	3	0	−1	1	−1
T_2	3	0	−1	−1	1

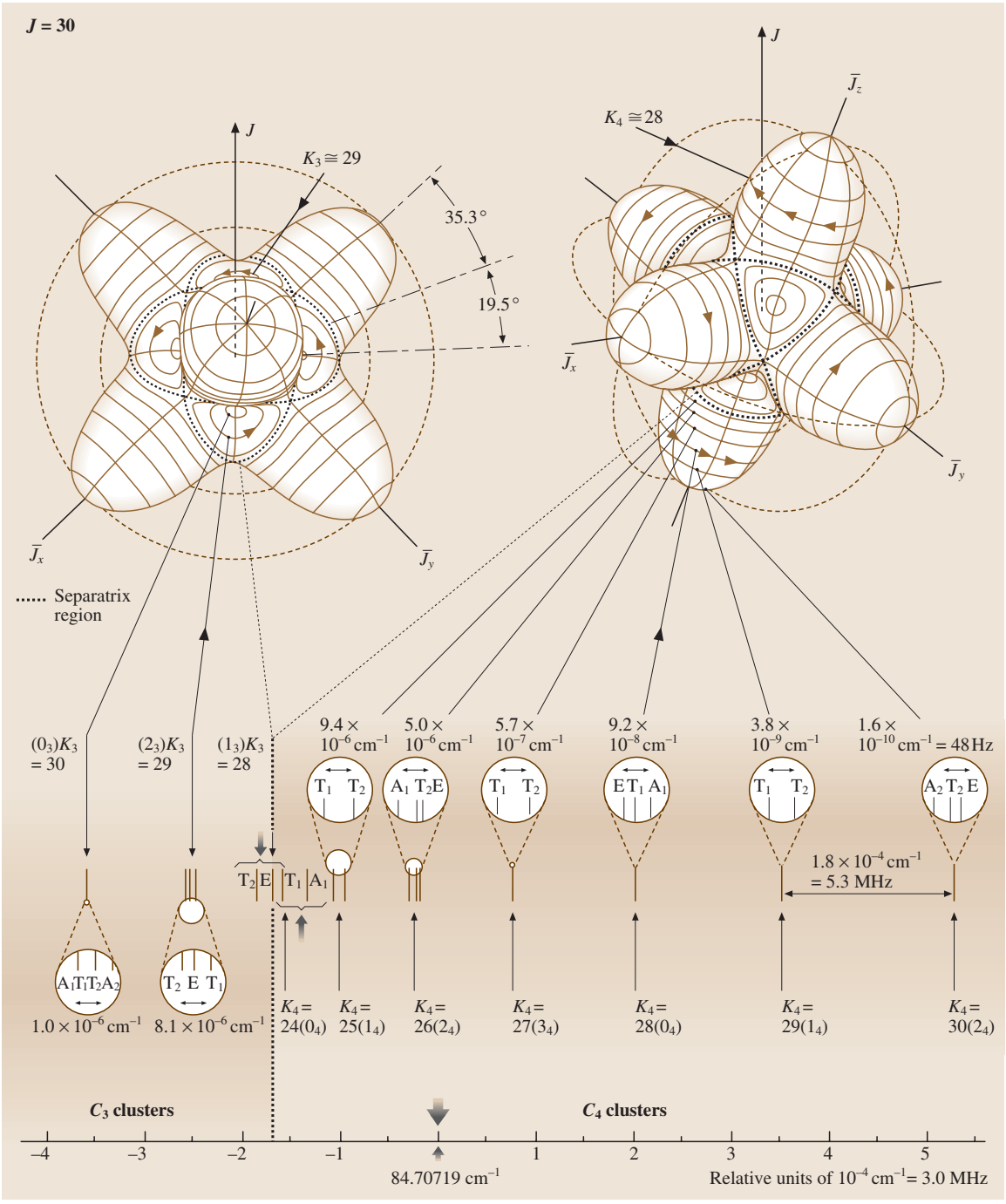

Fig. 32.4 $J = 10$ rotational energy surface related level spectrum for a semirigid octahedral or thetrahedral rotor

while T_1 and T_2 are triplets. These species form two clusters (A_1, T_1, T_2, A_2) and (T_2, E, T_1) on the low end of the spectrum and six clusters (T_1, T_2), (A_2, T_2, E), (T_1, T_2), (E, T_1, A_1), (T_1, T_2), and (A_2, T_2, E) on

the upper part of the spectrum. (See the right-hand side of Fig. 32.4). Note that the total dimension or (near) degeneracy for each of the two lower clusters is eight: $(1+3+3+1)$ and $(3+2+3)$, while the upper clusters each have a six-fold (near) degeneracy: $(3+3)$, $(1+3+2)$, etc.

Each of the two lower eight-fold clusters can be associated with semiclassical quantizing paths in an RES valley as shown in Fig. 32.4. The eight-fold dimension or (near) degeneracy occurs because each quantizing path is repeated eight times – once in each of the eight identical valleys. Similarly, the six-fold cluster dimension occurs because there are six identical hills, and each quantizing path is repeated six times around the surface.

The majority of the paths lie on the hills because the hills are bigger than the valleys. The hills subtend a half angle of 35.3° to the separatrix, while the valleys only have 19.5°. To estimate the number of paths or clusters in hills or valleys, the angular momentum cone angles for $J = 30$ may be calculated using (32.10). The results are displayed in Fig. 32.5. The results are consistent with the spectrum in Fig. 32.4. Only the two highest K-values of $K = 29, 30$ have cones small enough to fit in the valleys, but the six states of $K = 25–30$ can all fit onto the hills.

The angular momentum cone formula also provides an estimate for each level cluster energy. The estimates become more and more accurate as K increases (approaching J), while the uncertainty angle Θ_K^J decreases. Paths for higher K are more nearly circular and therefore more nearly correspond to symmetric top quantum states of pure K. The paths on octahedral RE surfaces are more nearly circular for a given K than are those on the asymmetric top RE surface, and so the octahedral rotor states can be better approximated by those of a symmetric top.

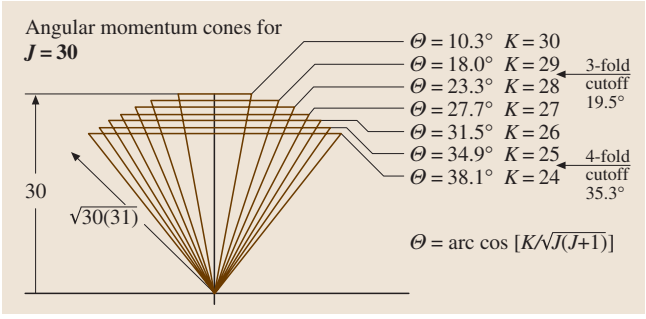

Fig. 32.5 $J = 30$ angular momentum cone half angles and octahedral cutoffs

32.4.4 Octahedral Superfine Structure

The octahedral RES has many more local hills and valleys and corresponding types of semiclassical paths than are found on the rigid asymmetric top RES. The tunneling between multiple paths produces an octahedral superfine structure that is more complicated than the asymmetric top doublets. Still, the same symmetry correlations and tunneling mechanics may be used.

First, the octahedral symmetry must be correlated with the local symmetry of the paths on the hills and in the valleys. The hill paths have a C_4 symmetry while the valley paths have a local C_3 symmetry. This is seen most clearly for the low-K paths near the separatrix which are less circular. The C_3 and C_4 correlations are given in Fig. 32.6 with a sketch of the corresponding molecular rotation for each type of path.

To find the octahedral species associated with a $K_3 = 30$ path in a C_3 valley one notes that 30 is 0 modulo 3. Hence the desired species are found in the 0_3 column of the C_3 correlation table: (A_1, A_2, T_1, T_2). This is what appears (not necessarily in that order) in the lower left corner of Fig. 32.4. Similarly, the species (A_2, E, T_2) for a $K_4 = 30$ path on top of a C_4 hill are found in the 2_4 column of the C_4 correlation table since 30 is 2 modulo 4; these appear on the other side of Fig. 32.4. Clusters (T_1, T_2) for $K_4 = 29$ and (A_1, E, T_1) for $K_4 = 28$ are found in a similar manner.

A multiple path tunneling calculation analogous to the one for rigid rotors can be applied to approximate octahedral superfine splittings. Consider the cluster (A_1, E, T_1) for $K_4 = 28$, for example. Six C_4-symmetric paths located on octahedral vertices on opposite sides of the x-, y-, and z-axes may be labeled $\{|x\rangle, |\bar{x}\rangle, |y\rangle, |\bar{y}\rangle, |z\rangle, |\bar{z}\rangle\}$. A tunneling matrix between the six paths follows:

$$\langle H\rangle_{K_4=28} = \begin{pmatrix} H & 0 & S & S & S & S \\ 0 & H & S & S & S & S \\ S & S & H & 0 & S & S \\ S & S & 0 & H & S & S \\ S & S & S & S & H & 0 \\ S & S & S & S & 0 & H \end{pmatrix} \begin{matrix} |x\rangle \\ |\bar{x}\rangle \\ |y\rangle \\ |\bar{y}\rangle \\ |z\rangle \\ |\bar{z}\rangle \end{matrix}, \tag{32.18}$$

where the tunneling amplitude between nearest neighbor octahedral vertices is S, but is assumed to be zero between antipodal vertices. The eigenvectors and eigenvalues for this matrix are given in the Table 32.5.

This predicts that the triplet (T_1) level should fall between the singlet (A_1) and the doublet (E) levels and the singlet-triplet spacing $(4S)$ should be twice the split-

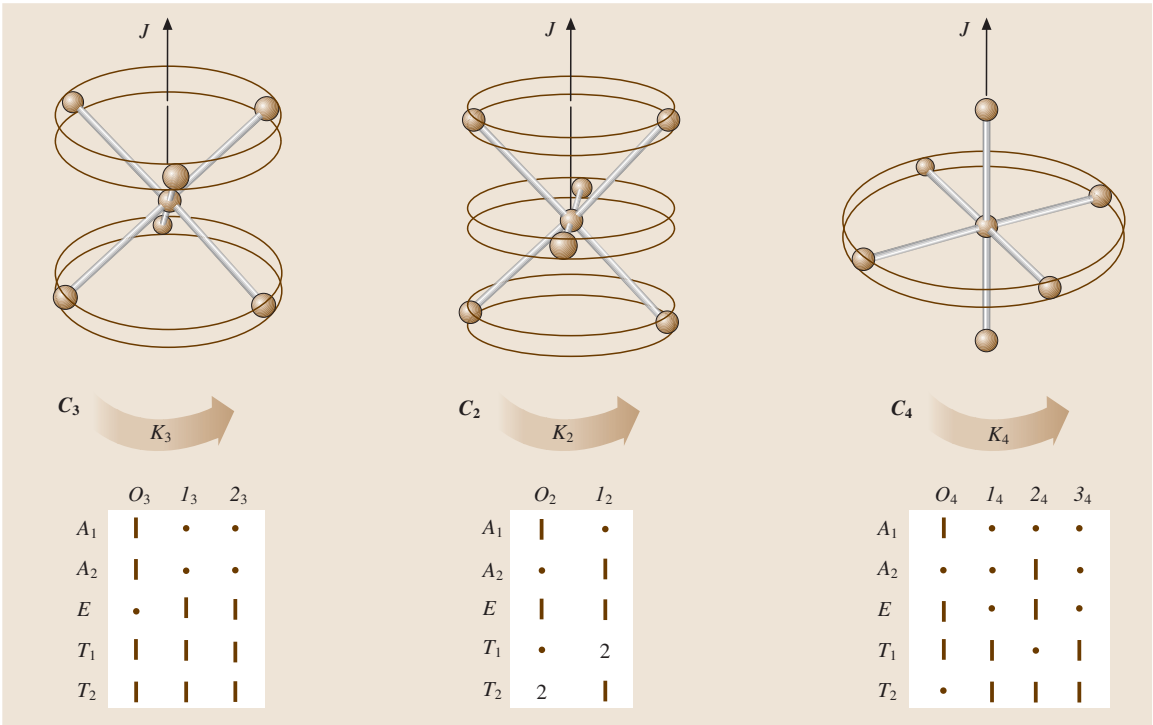

Fig. 32.6 Tables of correlations between 0 symmetry species and the cyclic axial symmetry species (K_p means K mod p) of subgroups C_3, C_2 and C_4

ting (-2S) between the triplet and doublet. This 2 : 1 ratio is observed in the (E, T_1, A_1) and (A_2, T_2, E) clusters which can be resolved and also in numerical calculation [32.18–21].

The tunneling amplitudes can be calculated by a separatrix path integral analogous to the asymmetric top formula (32.13) [32.10, 11]. As shown in Fig. 32.4, the tunneling rates or superfine splittings near the separatrix are ~ 1 MHz, which is only slightly slower than the classical precessional frequency. But as K approaches J on the hilltops, the tunneling rate slows down to a few Hz.

Table 32.5 Eigenvectors and eigenvalues of the tunneling matrix for the (A_1, E, T_1) cluster with $K = 28$

Eigenvector	$\|x\rangle$	$\|\overline{x}\rangle$	$\|y\rangle$	$\|\overline{y}\rangle$	$\|z\rangle$	$\|\overline{z}\rangle$	Eigenvalue
$\sqrt{6}\,\|A_1\rangle =$	1	1	1	1	1	1	$E^{A_1} = H + 4S$
$\sqrt{12}\,\|E,1\rangle =$	2	2	−1	−1	−1	−1	$E^{E} = H - 2S$
$2\,\|E,2\rangle =$	0	0	1	1	−1	−1	
$\sqrt{2}\,\|T_1,1\rangle =$	1	−1	0	0	0	0	$E^{T_1} = H$
$\sqrt{2}\,\|T_1,2\rangle =$	0	0	1	−1	0	0	
$\sqrt{2}\,\|T_1,3\rangle =$	0	0	0	0	1	−1	

32.5 High Resolution Rovibrational Structure

A display of spectral hierarchy for higher and higher resolution is shown in Fig. 32.7 for the 630 cm^{-1} or 16 μm bands of CF_4. This will serve to summarize the possible rovibrational spectral structures and place them in a larger context. The ν_4 resonance in part (a) corresponds to a dipole active $n_4 = 0 \rightarrow 1$ vibrational

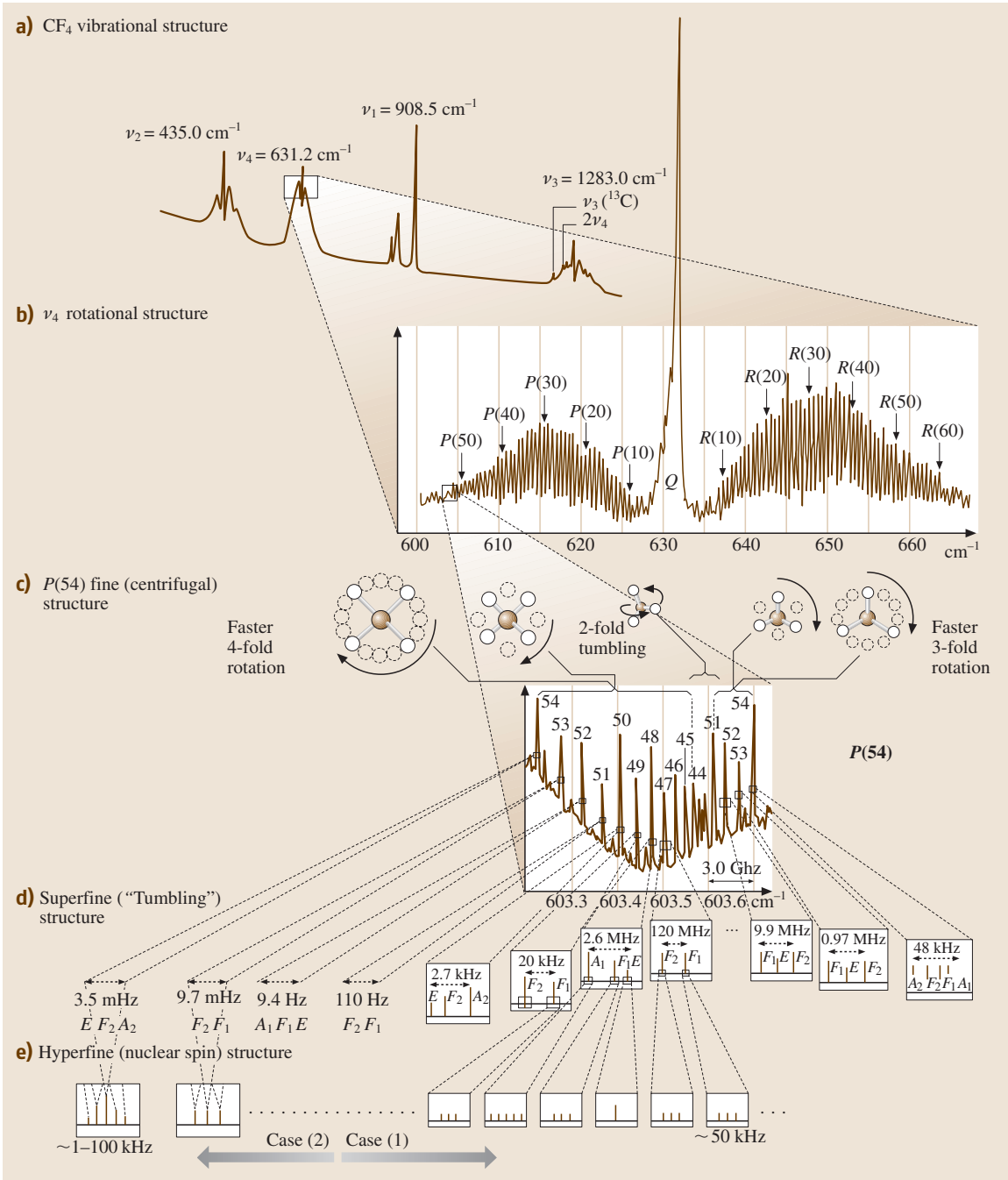

Fig. 32.7a–e Rovibrational structure in the 630 cm^{-1} or 16 μm bands of CF_4 [32.16]. **(a)** Vibrational resonances and band profiles. (Raman spectra from [32.23]). **(b)** Rotational P, Q, and R band structur corresponding to $J \rightarrow J-1$, $J \rightarrow J+1$ transitions. (FTIR spectra from [32.24]). **(c)** P(54) rotational fine structure due to rotation–vibration coupling and angular momentum precessional motion. (Laser diode spectra from [32.25]). **(d)** Superfine structure due to precessional tunneling [32.26]. **(e)** Hyperfine structure due to nuclear spin precession [32.26]

transition, and is just one of many vibrational structures to study. The $P(54)$ sideband resonance in part (b) corresponds to a $(J = 54) \rightarrow (J - 1)$ rotational transition, and is just one of hundreds of rotational structures to study within the ν_4 bands.

Each band is something like a Russian doll; it contains structure within structure within structure down to the resolution of few tens of Hz. Examples of rotational fine and superfine structures described in Sect. 32.4 are shown in Fig. 32.7c, d, but even more resolution is needed to see the hyperfine structure in Fig. 32.7e. Such extremely high resolution has been reached with a CO_2 saturation absorption spectrometer [32.27, 28]. The 10 μm bands of SF_6 and SiF_4 have been studied in this manner, the latter being similar to CF_4 [32.26].

32.5.1 Tetrahedral Nuclear Hyperfine Structure

High resolution spectral studies of SiF_4 showed unanticipated effects involving the four fluorine nuclear spin and magnetic moments and their associated hyperfine states. First, the Pauli principle restricts the nuclear spin multiplicity associated with each of the rotational symmetry species in much the same way that atomic $L - S$ coupled states ${}^{2S+1}L$ have certain spin multiplicities $(2S + 1)$ allowed for a given orbital L species involving two or more equivalent electrons. Second, since superfine splittings can easily be tiny, different spin species can end up close enough that hyperfine interactions, however small, can cause strongly resonant mixing of the normally inviolate species. Finally, a pure and simple form of spontaneous symmetry breaking is observed in which otherwise equivalent nuclei fall into different subsets due to quantum rotor dynamics.

Connecting nuclear spin to rotational species is done by correlating the full permutation symmetry (S_n for XY_n molecules) with the full molecular rotation and parity symmetry [$O(3)_{LAB} \otimes T_{dBODY}$ for CF_4 molecules or $O(3)_{LAB} \otimes O_{hBODY}$ and for SF_6]. For four spin-1/2 nuclei, the Pauli principle allows a spin of $I = 2$ and a spin multiplicity of five $(2I + 1 = 5)$ for (J^+, A_2) or (J^-, A_1) species, but excludes (J^-, A_2) or (J^+, A_1) species altogether. The Pauli allowed spin for (J^+, T_1) or (J^-, T_2) species is $I = 1$ with a multiplicity of three, but there are no allowed (J^+, T_2) or (J^-, T_1) species. Finally, both (J^+, E) and (J^-, E) belong to singlet spin $I = 0$ and are singlet partners to an inversion doublet. (None of the other species can have both + and − parity.)

The E inversion doublet is analogous to the doublet in NH_3 which is responsible for the ammonia maser. However, NH_3-type inversion is not feasible in CF_4 or SiF_4, and so the splitting of the E doublet in these molecules is due to hyperfine resonance [32.9, 16, 23].

The Pauli analysis gives the number of hyperfine lines that each species would exhibit if it were isolated and resolved, as shown in the center of Fig. 32.7e. The rotational singlets A_1 and A_2 have five lines each, the rotational triplets T_1 and T_2 are spin triplets, and the rotational doublet E is a spin singlet but an inversion doublet. If the hyperfine structure of a given species A_1, A_2, T_1, T_2, or E is not resolved, then their line heights are proportional to their total spin weights of 5, 5, 3, 3, and 2, respectively.

If the unresolved species are clustered, then the total spin weights of each add to give a characteristic cluster line height. The line heights of the C_4 clusters (T_1, T_2), (A_2, T_2, E), (T_1, T_2), (E, T_1, A_1) are 6, 10, 6, 10, respectively. The line heights of the C_3 clusters (A_1, T_1, T_2, A_2), (T_1, E, T_2), (T_1, E, T_2) are 16, 8, 8, respectively. This is roughly what is seen in the $P(54)$ spectrum in Fig. 32.7c.

32.5.2 Superhyperfine Structure and Spontaneous Symmetry Breaking

The superfine cluster splittings $(2S, 4S$, etc.) are proportional to the $\boldsymbol{J}$-precessional tunneling or 'tumbling' rates between equivalent C_3 or C_4 symmetry axes, and they decrease with increasing K_3 or K_4. At some point, the superfine splittings decrease to less than the hyperfine splittings which are actually increasing with K. The resulting collision of superfine and hyperfine structure has been called superhyperfine structure or Case 2 clusters. The following is a rough sketch of the phenomenology of this very complex effect, using the results of *Pfister* [32.26].

As long as the tunneling rates are > 1 MHz, the nuclear spins will tend to average over spherical top motion. The spins couple into states of good total nuclear spin I, which in turn couple weakly with the overall angular momentum and with well defined rovibrational species A_1, A_2, T_1, T_2, or E as described above. The resulting coupling is called Case 1, and is analogous to LS coupling in atoms.

Stick figures for two examples of spectra observed by *Pfister* [32.26] are shown in Fig. 32.8a and b. The first Case 1 cluster, shown in (a), is a C_4 type (0_4) cluster (A_1, T_1, E), which was solved in Table 32.6. The other Case 1 cluster, shown in (b), is a C_3 type $(\pm 1_3)$ cluster (T_1, E, T_2) (recall the C_3 correlations in Fig. 32.3). They are

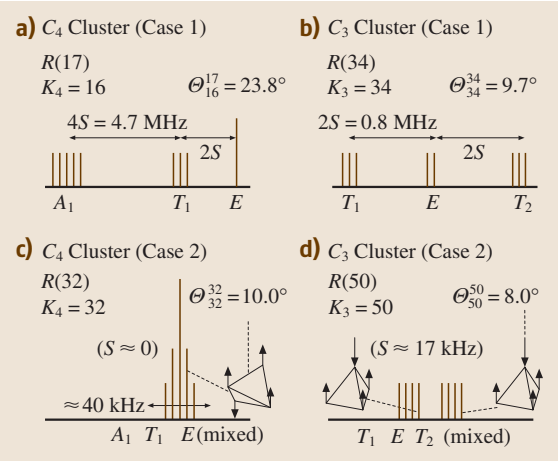

Fig. 32.8a–d Stick sketches for example of superfine and hyperfine spectral structure found by *Pfister* [32.26]; **(a)**,**(b)** Case 1 clusters (high tunneling amplitude S); **(c)**,**(d)** Case 2 clusters (low tunneling amplitude S)

similar to the corresponding sketches in Fig. 32.7e. One notable difference is that the inversion doublet shows little or no splitting in the (A_1, T_1, E) cluster, but does split in the (T_1, E, T_2) cluster.

When the tunneling rates fall below 10 or 20 kHz, the angular momentum can remain near a particular C_3 or C_4 symmetry axis for a time longer than the nuclear spin precession rates. Spin precession rates and the corresponding hyperfine splittings are ≈ 50 kHz, and increase with K. Hence, there is plenty of time for each of the nuclear spins to align or anti-align with the C_3 or C_4 symmetry axes of rotation. This is called Case 2 coupling, and the resulting spectrum resembles that of an NMR scan of the nuclei, but here the magnetic field is provided by the molecule's own body frame rotation.

If SiF_4 rotates uniformly about one C_4 symmetry axis, then all four F nuclei occupy equivalent positions at the same average distance from the rotation axis and experience the same local magnetic fields. The molecule can be thought of as a paired diatomic F_2–F_2 rotor with each one symmetrized or antisymmetrized so as to make the whole state symmetric. Table 32.6 shows the spin-$^1/_2$ base states arranged horizontally according to the total projection I_z of nuclear spins on the C_4 axis. Horizontal arrays ($\uparrow\downarrow$) of spins denote symmetric states, while vertical arrays ($\updownarrow$) denote antisymmetric spin states.

The hyperfine energy is approximately proportional to the projection I_z. The resulting spectrum

Table 32.6 Spin $-\frac{1}{2}$ basis states for SiF_4 rotating about a C_4 symmetry axis

$I_z = 2$	$I_z = 1$	$I_z = 0$	$I_z = -1$	$I_z = -2$
		$\left\vert \begin{matrix}\uparrow & \uparrow \\ \downarrow & \downarrow\end{matrix} \right\rangle$		
		$\vert\uparrow\downarrow\ \uparrow\downarrow\rangle$		
	$\vert\uparrow\downarrow\ \uparrow\uparrow\rangle$	$\vert\downarrow\downarrow\ \uparrow\uparrow\rangle$	$\vert\downarrow\downarrow\ \uparrow\downarrow\rangle$	
$\vert\uparrow\uparrow\ \uparrow\uparrow\rangle$	$\vert\uparrow\uparrow\ \uparrow\downarrow\rangle$	$\vert\uparrow\uparrow\ \downarrow\downarrow\rangle$	$\vert\uparrow\downarrow\ \downarrow\downarrow\rangle$	$\vert\downarrow\downarrow\ \downarrow\downarrow\rangle$

is (1, 2, 4, 2, 1)-degenerate pyramid of equally spaced lines as shown in Fig. 32.8c. Four spin-1/2 states without symmetry restrictions would give the standard binomial (1, 4, 6, 4, 1)-degeneracy seen in NMR spectra.

If the molecule settles upon C_3 symmetry axes of rotation, the situation is markedly different. The four nuclei no longer occupy equivalent positions. One nucleus sits on the rotation axis, while the other three nuclei occupy equivalent off-axis positions. The off-axis nuclei experience a different local magnetic field than the single on-axis nucleus (Fig. 32.8d). From the spectrum, it appears that the spin-up to spin-down energy difference is much greater for the lone on-axis nucleus than for the three equatorial nuclei, whose spin states form the energy quartet $\{|\uparrow\uparrow\uparrow\rangle, |\uparrow\uparrow\downarrow\rangle, |\uparrow\downarrow\downarrow\rangle, |\downarrow\downarrow\downarrow\rangle\}$. The on-axis nucleus has an energy doublet with a large splitting, so that the four nuclei together give a doublet of quartets as shown in the figure.

If the off-axis nuclei had experienced the greatest splitting, then the spectrum would have been a quartet of doublets instead of a doublet of quartets. Something like this does occur in the SF_6 superhyperfine structure, which shows a quintet of triplets for a Case-2 C_4-symmetry cluster. For either one of these molecules, it is remarkable how different the rovibrational 'chemical shifts' can become for equivalent symmetry sites. The result is a microscopic example of spontaneous symmetry breaking.

32.5.3 Extreme Molecular Symmetry Effects

The most common high symmetry molecules belong to either the tetrahedral T_d or cubic-octahedral O groups. Until the recent discovery of fullerenes and the structure of virus coats, the occurrence of molecular point groups of icosahedral symmetry was thought to be rare or nonexistent in nature [32.24, 25].

For an extreme example of symmetry breaking effects, consider the Buckminsterfullerene or Buckyball molecule C_{60} which has the highest possible molecular point symmetry Y_h. A semiclassical approach to rota-

tional symmetry and dynamics is useful here since the rotational quantum constant is so small for the fullerenes (for C_{60} $2B = 0.0056\,\mathrm{cm}^{-1}$ or 168 MHz) [32.29–31].

Since there are two isotopes ^{12}C (nuclear spin 0) and ^{13}C (nuclear spin 1/2) it is possible to have a Bose-symmetric molecule ($^{12}C_{60}$), or Fermi-symmetric molecule ($^{13}C_{60}$), or many broken-symmetry combinations ($^{12}C_x\,^{13}C_{60-x}$). The most likely combination is $^{12}C_{59}\,^{13}C$, which has no rotational symmetry at all, only one reflection plane. This may be the most extreme example of molecular isotopic symmetry breaking; it goes from the highest possible symmetry Y_h to one of the lowest, C_h.

The Fermi-symmetric molecule $^{13}C_{60}$ has ten times as many rotating spin-1/2 nuclei as SF_6, and 2^{10} times as many hyperfine states, or about 1.15×10^{18} spin states distributed among 10 symmetry species [32.32]. In contrast,the Bose-symmetric molecule $^{12}C_{60}$ has only one spin symmetry species allowed by the Bose exclusion principle: A_{1g}. It provides an even more extreme example of Bose exclusion than the $Os^{16}O_4$ molecule. In all, 119 of the 120 Y_h rovibrational symmetry states are Bose-excluded, giving $^{12}C_{60}$ an extraordinarily sparse rotational structure. However, it only takes the addition of a single neutron to make $^{12}C_{59}\,^{13}C$. Then all the excluded rovibrational states must return!

32.6 Composite Rotors and Multiple RES

So far, the discussion has focused on Hamiltonians and RES involving functions of even mulipolarity, i. e., constant ($k=0$), quadrupole ($k=2$), hexadecapole ($k=4$), while ignoring odd functions, i. e., dipole ($k=1$), octupole ($k=3$), for reasons of time-reversal symmetry. However, for composite "rotor-rotors" any mulitpolarity is possible, and the dipole is of primary utility.

A composite rotor is one composed of two or more objects with more or less independent angular momenta. This could be a molecule with attached methyl (CH_3) "gyro" or "pinwheel" sub-rotors, a system of considerable biological interest. It could be a molecule with a vibration or "phonon" excitation that couples strongly to rotation. Also, any nuclear or electronic spin with significant coupling may be regarded as an elementary sub-rotor. The classical analogy is a spacecraft with gyros on board.

A rotor–rotor Hamiltonian has the general interaction form

$$H_{\mathrm{rotor}\ R+S} = H_{\mathrm{rotor}_R} + H_{\mathrm{rotor}_S} + V_{RS}\,. \tag{32.19}$$

A useful approximation assumes that rotor S, the "gyro", is fastened to the frame of rotor R, so that the interaction V_{RS} becomes a constraint, does no work, and is thus assumed to be zero. An asymmetric top with body-fixed spin has the Hamiltonian

$$\begin{aligned} H_{R+S(\mathrm{Body\text{-}fixed})} &= A\boldsymbol{R}_x^2 + B\boldsymbol{R}_y^2 + C\boldsymbol{R}_z^2 + H_{\mathrm{rotor}_S} \\ &\quad + (\sim 0)\,, \end{aligned} \tag{32.20a}$$

which is a modified version of (32.1). The total angular momentum of the system is a conserved vector $\boldsymbol{J} = \boldsymbol{R} + \boldsymbol{S}$ in the lab-frame and a conserved magnitude $|\boldsymbol{J}|$ in the rotor-R body frame. So we use $\boldsymbol{R} = \boldsymbol{J} - \boldsymbol{S}$ in place of $\boldsymbol{R}$:

$$\begin{aligned} H_{R,S(\mathrm{fixed})} &= A\,(\boldsymbol{J}_x - \boldsymbol{S}_x)^2 + B\left(\boldsymbol{J}_y - \boldsymbol{S}_y\right)^2 \\ &\quad + C\,(\boldsymbol{J}_z - \boldsymbol{S}_z)^2 + H_{\mathrm{rotor}_S} \\ &= A\boldsymbol{J}_x^2 + B\boldsymbol{J}_y^2 + C\boldsymbol{J}_z^2 - 2A\boldsymbol{J}_x\boldsymbol{S}_x \\ &\quad - 2B\boldsymbol{J}_y\boldsymbol{S}_y - 2C\boldsymbol{J}_z\boldsymbol{S}_z + H'_{\mathrm{rotor}_S}\,. \end{aligned} \tag{32.20b}$$

The gyro spin components $\boldsymbol{S}_a$ are first treated as constant classical parameters S_a:

$$\begin{aligned} H_{R,S(\mathrm{fixed})} &= \mathrm{const.}\,1 - 2AS_x\boldsymbol{J}_x - 2\mathrm{B}S_y\boldsymbol{J}_y - 2CS_z\boldsymbol{J}_z \\ &\quad + A\boldsymbol{J}_x^2 + B\boldsymbol{J}_y^2 + C\boldsymbol{J}_z^2 \\ &= M_0\boldsymbol{T}_0^0 + \sum\nolimits_d D_d\boldsymbol{T}_d^1 + \sum\nolimits_q Q_q\boldsymbol{T}_q^2\,. \end{aligned} \tag{32.20c}$$

This is a simple Hamiltonian multipole tensor operator expansion having here just a monopole $\boldsymbol{T}_0^0$ term, three dipole $\boldsymbol{T}_a^1$ terms, and two quadrupole $\boldsymbol{T}_q^2$ terms. Figure 32.9 shows these three tensor terms, where each graph is a radial plot of a spherical harmonic function $Y_q^k(\phi, \Phi)$ representing a tensor operator $\boldsymbol{T}_q^k$. The tensor components are

$$\boldsymbol{T}_0^0 = \frac{\boldsymbol{J}_x^2 + \boldsymbol{J}_y^2 + \boldsymbol{J}_z^2}{3} \tag{32.21a}$$

$$\begin{aligned} \boldsymbol{T}_x^1 &= \boldsymbol{J}_x = \frac{\boldsymbol{T}_{+1}^1 + \boldsymbol{T}_{-1}^1}{\sqrt{2}} \\ \boldsymbol{T}_y^1 &= \boldsymbol{J}_y = \frac{\boldsymbol{T}_{+1}^1 - \boldsymbol{T}_{-1}^1}{\mathrm{i}\sqrt{2}} \\ \boldsymbol{T}_z^1 &= \boldsymbol{J}_z = \boldsymbol{T}_0^1 \end{aligned} \tag{32.21b}$$

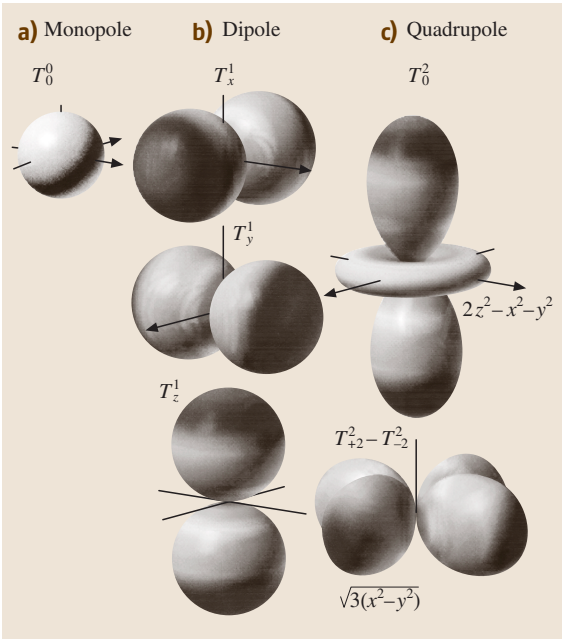

Fig. 32.9a–c The six lowest order RES components needed to describe rigid gyro-motors

$$T^2_{zz} = \frac{2J_z^2 - J_x^2 - J_y^2}{2} = T^2_0$$

$$T^2_{x^2-y^2} = J_x^2 - J_y^2 = \frac{2\left(T^2_2 - T^2_{-2}\right)}{\sqrt{6}} \qquad (32.21c)$$

The constant coefficients or moments indicate the strength of each multipole symmetry:

$$M_0 = A + B + C + 3H'_{\text{rotor}_S} \qquad (32.22a)$$

$$D_x = -2AS_x\,,$$

$$D_y = -2BS_y\,,$$

$$D_z = -2CS_z \qquad (32.22b)$$

$$Q_{zz} = (2C - A - B)/6$$

$$Q_{x^2-y^2} = (A - B)/2 \qquad (32.22c)$$

The scalar monopole RES (a) is a sphere, the vector dipole RES (b) are bi-spheres pointing along Cartesian axes, and the RES (c) resemble quadrupole antenna patterns. Also, Fig. 32.9a–c plot the six s, p, and d Bohr–Schrödinger orbitals that are analogs for the six octahedral J-tunneling states listed in Table 32.5.

The asymmetric and symmetric rotor Hamiltonians (32.1) and (32.1) are combinations of a monopole (32.21a), which by itself makes a spherical rotor, and varying amounts of the two quadrupole terms (32.21c) to give the rigid rotor RES pictured in Figs. 32.1 and Fig. 32.2. The Q coefficients in (32.22c) are both zero for a spherical top ($A = B = C$), but only one is zero for a symmetric top ($A = B$).

Combining the monopole (32.21a) with the dipole terms (32.21b) gives the gyro-rotor Hamiltonian (32.20b) for a spherical rotor ($A = B = C$):

$$H = \text{const} + BJ^2 - g\mu \boldsymbol{S}\cdot\boldsymbol{J}\,, \qquad (32.23)$$

where $-g\mu = 2A = 2B = 2C$. This Hamiltonian resembles a dipole potential $-\boldsymbol{m}\cdot\boldsymbol{B}$ for a magnetic moment $\boldsymbol{m} = g\boldsymbol{J}$ that precesses clockwise around a lab-fixed magnetic field $\boldsymbol{B} = \mu\boldsymbol{S}$. (The PE is least for $\boldsymbol{J}$ along $\boldsymbol{S}$.)

The Hamiltonian (32.23) is a simple example of Coriolis rotational energy. It is least for $\boldsymbol{J}$ along $\boldsymbol{S}$, where $|\boldsymbol{R}| = |\boldsymbol{J} - \boldsymbol{S}|$ and the rotor kinetic energy BR^2 are least. (Magnitudes $|J|$ and $|S|$ are constant here.) The spherical rotor-gyro RES in Fig. 32.10 has a minimum along the body-axis $+\boldsymbol{S}$ and a maximum along $-\boldsymbol{S}$, where BR^2 is greatest.

As is the case for the rigid solid rotors in Figs. 32.1 and Fig. 32.2, the RES topography lines determine the precession $\boldsymbol{J}$-paths in the body frame, wherein gyro-$\boldsymbol{S}$ is fixed, as shown in Fig. 32.10. The left-hand rule gives the sense of the $\boldsymbol{J}$-precession in the body $\boldsymbol{S}$-frame, i. e., all $\boldsymbol{J}$ precess counterclockwise relative to the "low" on the $+\boldsymbol{S}$-axis, or clockwise relative to the "high" on the $-\boldsymbol{S}$-axis. In the lab, $\boldsymbol{S}$ precesses in a clockwise manner around a fixed $\boldsymbol{J}$.

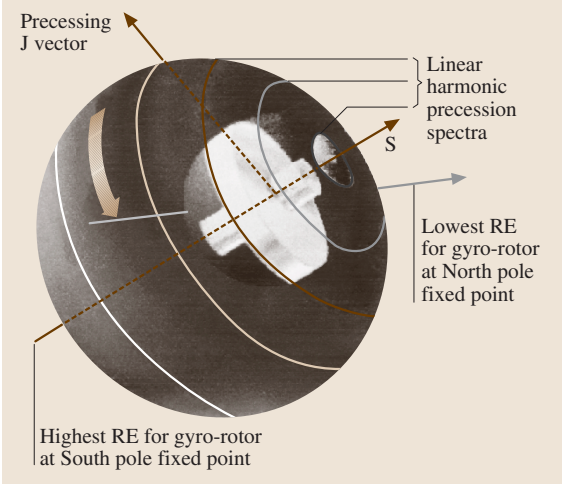

Fig. 32.10 The spherical gyro-rotor RES is a cardioid of revolution around gyro spin $\boldsymbol{S}$

Gyro-RES differ from solid rotor RES, which have two opposite "highs" and/or two opposite "lows" separated by saddle fixed points where the precessional flow direction reverses, as seen in Fig. 32.2. The gyro-RES in Fig. 32.10 has no saddle fixed points, and thus has only one "high" and one direction of flow with the same harmonic precession frequency for all $\boldsymbol{J}$-vectors between the high $+\boldsymbol{S}$ and low $-\boldsymbol{S}$-axes. This is because the spectrum of the gyro-rotor Hamiltonian (32.23) is harmonic, or linear, in the K:

$$\left\langle \begin{matrix} J \\ K \end{matrix} \middle| H \middle| \begin{matrix} J \\ K \end{matrix} \right\rangle = \text{const.} + BJ(J+1) - 2BK \,. \qquad (32.24)$$

In contrast, even the symmetric rigid rotor spectrum (32.4) is quadratic in K. Other rotors shown in Figs. 32.2 and Fig. 32.4 have levels that have an even more nonlinear spacing.

32.6.1 3D-Rotor and 2D-Oscillator Analogy

Linear levels are usually associated with harmonic oscillators not rotors, but the gyro-rotor's linear spectrum highlights a 160-year-old analogy between the motions of 3D rotors and 2D vibrations [32.33–45]. Stokes [32.35] first described 2D electric vibration or optical polarization, by a 3D vector that became known as the Stokes vector $\boldsymbol{S}$, and later as the "spin" $\boldsymbol{S}$. The Stokes spin was based on Hamilton's quaternions q_μ [32.33,34]. The Pauli spinors $\sigma_\mu = \mathrm{i}q_\mu$ [32.36] were defined, 83 years later, as components of a general 2D Hermitian matrix H. Spinors square to the unit matrix $\left(\sigma_\mu^2 = \boldsymbol{1} = \sigma_0\right)$, while quaternions square to $-\boldsymbol{1}$. The 3D Hamiltonian is

$$\begin{aligned} H &= \begin{pmatrix} A & B - \mathrm{i}C \\ B + \mathrm{i}C & D \end{pmatrix} \\ &= \frac{A+D}{2}\sigma_0 + \frac{A-D}{2}\sigma_\mathrm{A} + B\sigma_\mathrm{B} + C\sigma_\mathrm{C} \,, \end{aligned} \qquad (32.25)$$

where

$$\sigma_0 = \begin{pmatrix} 1 & 0 \\ 0 & 1 \end{pmatrix} , \quad \sigma_\mathrm{A} = \begin{pmatrix} 1 & 0 \\ 0 & -1 \end{pmatrix} ,$$
$$\sigma_\mathrm{B} = \begin{pmatrix} 0 & 1 \\ 1 & 0 \end{pmatrix} , \quad \sigma_\mathrm{C} = \begin{pmatrix} 0 & -\mathrm{i} \\ i & 0 \end{pmatrix} .$$

The 3D-component labels $\frac{A-D}{2}$ (Asymmetric-diagonal), B (Bilateral-balanced), and C (Circular-Coriolis) are ABC mnemonics for Pauli's z, x, and y, respectively. The 2D operator H has a $\boldsymbol{1} + \boldsymbol{S}\cdot\boldsymbol{J}$ form of the Coriolis coupling Hamiltonian (32.23):

$$\begin{aligned} H &= S_0\boldsymbol{1} + S_A J_A + S_\mathrm{B} J_\mathrm{B} + S_\mathrm{C} J_\mathrm{C} \\ &= S_0 J_0 + \boldsymbol{S}\cdot\boldsymbol{J} \,, \end{aligned} \qquad (32.26)$$

where

$$J_0 = \boldsymbol{1} \,, \quad J_A = \frac{\sigma_A}{2} \,, \quad J_\mathrm{B} = \frac{\sigma_\mathrm{B}}{2} \,, \quad J_\mathrm{C} = \frac{\sigma_\mathrm{C}}{2} \,,$$

and

$$S_0 = (A+\mathrm{D})/2 \,, \quad S_A = (A-\mathrm{D}) \,, \quad S_\mathrm{B} = 2\mathrm{B} \,,$$
$$S_\mathrm{C} = 2\mathrm{C} \,.$$

The elementary 2D-oscillator ladder operators $a^\dagger$, and a make the 2D-3D theory more powerful. This is known as the Jordan–Schwinger map [32.37–39] between 2D oscillation and 3D rotation. In terms of the ladder operators

$$\begin{aligned} &\boldsymbol{J}_0 = \boldsymbol{N} = a_1^\dagger a_1 + a_2^\dagger a_2 \,, \; \boldsymbol{J}_A = \frac{1}{2}\left(a_1^\dagger a_1 - a_2^\dagger a_2\right) \,, \\ &\boldsymbol{J}_\mathrm{B} = \frac{1}{2}\left(a_1^\dagger a_2 + a_2^\dagger a_1\right) \,, \; \boldsymbol{J}_\mathrm{C} = \frac{-\mathrm{i}}{2}\left(a_1^\dagger a_2 - a_2^\dagger a_1\right) \,. \end{aligned} \qquad (32.27)$$

where

$$a_1^\dagger a_1 = \begin{pmatrix} 1 & 0 \\ 0 & 0 \end{pmatrix} , \; a_1^\dagger a_2 = \begin{pmatrix} 0 & 1 \\ 0 & 0 \end{pmatrix} ,$$
$$a_2^\dagger a_1 = \begin{pmatrix} 0 & 0 \\ 1 & 0 \end{pmatrix} , \; a_2^\dagger a_2 = \begin{pmatrix} 0 & 0 \\ 0 & 1 \end{pmatrix} .$$

The $a^\dagger a$-algebra gives Schwinger's 3D angular momentum raising and lowering operators $\boldsymbol{J}_+ = \boldsymbol{J}_\mathrm{B} + \mathrm{i}\boldsymbol{J}_\mathrm{C} = a_1^\dagger a_2$ and $\boldsymbol{J}_- = \boldsymbol{J}_\mathrm{B} - \mathrm{i}\boldsymbol{J}_\mathrm{C} = a_2^\dagger a_1$, where in two dimensions 1 and 2 are spin-up $(+\hbar/2)$ and spin-down $(-\hbar/2)$, instead of the x-and y-polarized states envisioned by Stokes.

The angular 3D ladder operation is replaced by a simpler 2D oscillator operation:

$$\begin{aligned} &\boldsymbol{J}_+ |n_1 n_2\rangle = {a_1}^\dagger a_2 \, |n_1 n_2\rangle = \\ &\quad \sqrt{n_1+1}\sqrt{n_2}\, |n_1+1, n_2-1\rangle \,, \\ &\boldsymbol{J}_- \, |n_1 n_2\rangle = a_2^\dagger a_1 \, |n_1 n_2\rangle = \\ &\quad \sqrt{n_1}\sqrt{n_2+1}\, |n_1-1, n_2+1\rangle \,. \end{aligned} \qquad (32.28)$$

The 2D oscillator states are labeled by the total number $N = (n_1 + n_2)$ of quanta and the net quantum population $\Delta N = (n_1 - n_2)$. The 3D angular momentum states $\left|\begin{matrix} J \\ K \end{matrix}\right\rangle$ are labeled by the total momentum $J = N/2 = (n_1 + n_2)/2$ and the z-component

$K = \Delta N/2 = (n_1 - -n_2)/2$, just half (or $\eta/2$) of N and ΔN.

$$|n_1, n_2\rangle = \frac{\left(a_1^\dagger\right)^{n_1}\left(a_2^\dagger\right)^{n_2}}{\sqrt{n_1! n_2!}}\,|0,0\rangle = \left|\begin{matrix} J \\ K \end{matrix}\right\rangle = \frac{\left(a_1^\dagger\right)^{J+K}\left(a_2^\dagger\right)^{J-K}}{\sqrt{(J+K)!\,(J-K)!}}\,|0,0\rangle \ , \qquad (32.29)$$

where

$$n_1 = J + K \ , \quad n_2 = J - K \ .$$

From this *Schwinger* [32.38] rederived the Wigner matrices $D^J_{MK}(\alpha\beta\gamma)$, which appear in (32.5) and (32.6), and the Wigner–Eckart or Clebsch–Gordan matrix values. This helps clarify the approximation of these values by $(J, K)-$cone levels around RES hills or valleys [recall (32.10) and (32.11)], since

$$\left\langle \begin{matrix} J' \\ K \end{matrix} \left| T^k_0 \right| \begin{matrix} J \\ K \end{matrix} \right\rangle = C^{kJJ}_{0KK}\,\langle J \,\|k\|\, J\rangle \sim D^J_{JK}\left(\Theta^J_K\right) \ .$$

32.6.2 Gyro-Rotors and 2D-Local Mode Analogy

The 2D–3D analogy provides insight into spin [32.40–42] and rovibrational dynamics [32.40–45], as well as having computational value. Consider extending a single 2D-oscillator-rotor analogy in the Stokes model to a model of two 1D oscillators with coordinates $x_1 = x$ and $x_2 = y$.

Identical side-by-side oscillators have bilateral B-symmetry. The Hamiltonian H_B commutes with the matrices σ_B ($+45°$ mirror reflection of axes $\pm x \leftrightarrows \pm y$) and $-\sigma_B$ ($-45°$ mirror reflection of axes $\mp x \leftrightarrows \pm y$), both of which switch oscillators. A first-order bilateral Hamiltonian is $H_B = 2B\sigma_B$. This is analogous to a gyro rotor $\boldsymbol{T}^1_x$ with $\boldsymbol{S}$ along the B-axis, as shown in Fig. 32.11a. (The added unit operator $\boldsymbol{T}^0_0$ shifts levels, but does not affect eigenstates.)

The eigenstates of H_B are the symmetric and antisymmetric normal modes that belong to the fixed points on the $\boldsymbol{S}$-vector or $\pm B$-axes of the 3D Stokes space. If instead, the $\boldsymbol{S}$-vector lies on the A-axis, the Hamiltonian is an asymmetric diagonal $H_A = 2A\sigma_A$ matrix. From (32.25) we see that the operator σ_A reflects y into $-y$ but leaves x alone, so that the eigenvectors of H_A are localized on the x-oscillator or the y-oscillator, but not on both. Such motions are local modes, but they are not modes of H_B since it does not commute with H_A.

If the vector $\boldsymbol{J}$ is on the $+A$-axis (local x-mode), the Hamiltonian H_B rotates $\boldsymbol{J}$ to the $-C$-axis, then to the $-A$-axis (local y-mode), then to the $+C$-axis, and then back to the $+A$-axis. This $\boldsymbol{J}$-path is the equator of Fig. 32.11a. The $\pm C$-axes label circular polarization with right and left chirality, respectively. Twice during a B-beat, $\boldsymbol{J}$ passes the $\pm C$-axes, where one vibrator's phase is 90° ahead and resonantly pumping

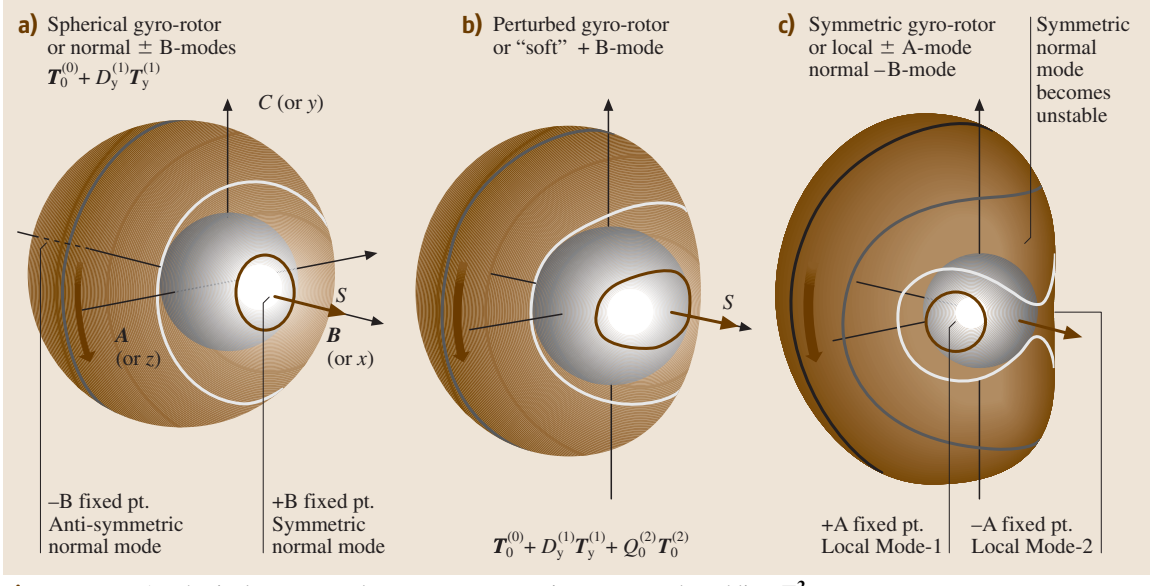

Fig. 32.11a–c A spherical gyro-rotor becomes a symmetric gyro-rotor by adding $\boldsymbol{T}^2_0$

the other. Such bilateral beat and resonant transfer is disrupted by adding anharmonic T_0^2 or $T_{\pm 2}^2$ terms to the B-symmetry terms T_x^1 and T_0^0. Adding T_0^2 causes B-circles in Fig. 32.11(a) to distort near the B-axis, as shown in Fig. 32.11b–c.

In molecular rotation theory, the T_0^2 and T_0^0 terms comprise the initial unperturbed Hamiltonian (32.3) of a symmetric top, while the gyro terms T_q^1 are viewed as perturbations in (32.20), due to an "on-board" gyro rotor. For vibration theory, the T_q^1 terms make up a normal-mode Hamiltonian, and the T_0^2 term is viewed as an anharmonic perturbation.

The effect of T_0^2, seen in Fig. 32.11c, is to replace the stable fixed point $+B$ (representing the (+)-normal mode) by a saddle point as B bifurcates (splits) into a pair of fixed points that head toward the $\pm A$-axes. So one normal mode dies and begets two stable local modes, wherein one mass may keep its energy, and not lose it to the other through the usual B-beating process. (The A-modes become anharmonically detuned.)

Pairs of classical modes, each localized on different sides of the RES in Fig. 32.11, are analogous to the asymmetric top $\pm K$-precession pairs in Fig. 32.2 with degenerate energy in a classical RES picture. The quantum-tunneling Hamiltonian (32.15) splits each trajectory pair into a superfine doublet with (±)-eigenstates sharing both RES paths, as seen in Table 32.1. The quantum gyro-spin doublets also share $\pm \boldsymbol{J}$ components both up and down the A-axis, as seen in Fig. 32.11c.

32.6.3 Multiple Gyro-Rotor RES and Eigensurfaces

While simple quantum rotors delocalize $\boldsymbol{J}$ to multiple RES paths, a gyro-rotor $\boldsymbol{J}$ may delocalize to multiple paths and surfaces. Gyro-rotor RES vary with $\boldsymbol{S}$, and if $\boldsymbol{S}$ is a quantum spin, the possibility arises for a distribution over multiple RES [32.46, 47]. A simple quantum theory of $\boldsymbol{S}$ allows both $+\boldsymbol{S}$ and $-\boldsymbol{S}$ at once. The RES for each is plotted one on top of the other, as in Fig. 32.12a, while component RES are shown in Fig. 32.12b for $+\boldsymbol{S}$ and in Fig. 32.12c for $-\boldsymbol{S}$. An energy sphere is shown intersecting an RES pair for an asymmetric gyro-rotor. If the spin $\boldsymbol{S}$ is set to zero, the pair of RES collapses into a rigid asymmetric top RES, shown in Fig. 32.2, having angular inversion (time-reversal $\boldsymbol{J} \to -\boldsymbol{J}$) and D_{2h} reflection symmetry. The composite RES in Fig. 32.12a has inversion symmetry, but lacks reflection symmetry. Its parts in Fig. 32.12b and c have neither inversion nor reflection symmetry if gyro-spins $\pm \boldsymbol{S}$ are off-axis.

The gyro-rotor Hamiltonian (32.20) allows tunneling or mixing of multiple RES. A two-state spin−1/2 gyro-spin model has a $2 \otimes 2$ Hamiltonian matrix and two base-RES:

$$H_{\text{gyro}} = M_0 \boldsymbol{J} \cdot \boldsymbol{J} + D_x S_x \boldsymbol{J}_x + D_y S_y \boldsymbol{J}_y + D_z S_z \boldsymbol{J}_z + Q_{xx} \boldsymbol{J}_x^2 + Q_{yy} \boldsymbol{J}_y^2 + Q_{zz} \boldsymbol{J}_z^2 \qquad (32.30)$$

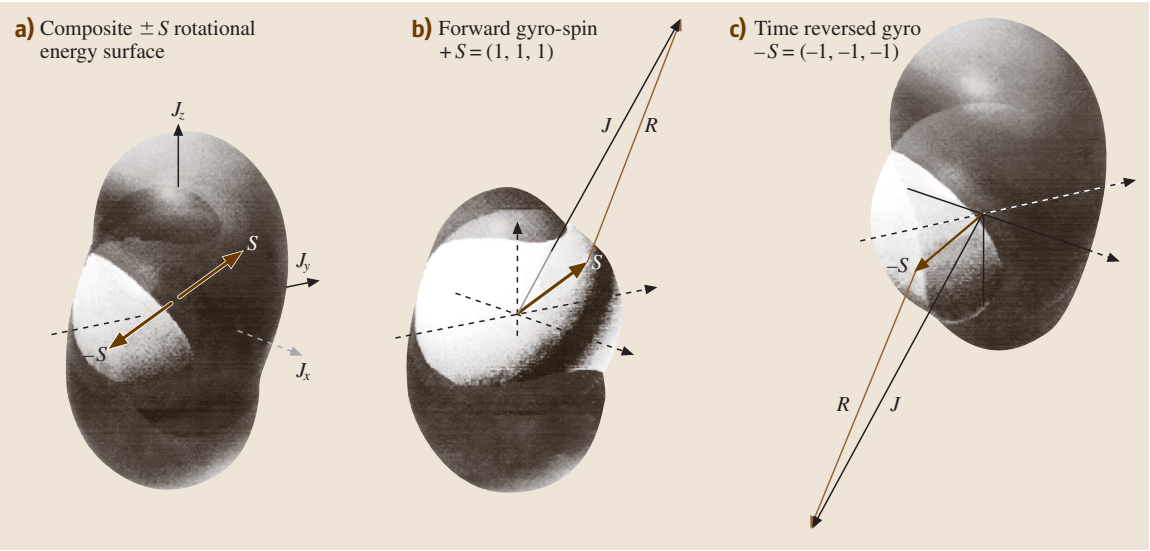

Fig. 32.12a–c Asymmetric gyro-rotor RES (classical body-fixed-spin case); **(a)** Composite $\pm \boldsymbol{S}$; **(b)** Forward spin $\pm \boldsymbol{S}$; **(c)** Reversed spin $-\boldsymbol{S}$

As in (32.7), $\boldsymbol{J}$ is approximated by classical vector components in the body frame:

$$\left(J_x = |J| \sin\beta\cos\gamma\,, \quad J_y = |J| \sin\beta\sin\gamma\,, \right.$$
$$\left. J_z = |J| \cos\beta\right)\,. \tag{32.31a}$$

But the gyro-spin S uses its quantum representation $\boldsymbol{S} = |S|\boldsymbol{\sigma}/2 = \sqrt{3}\boldsymbol{\sigma}/2$ from (32.25):

$$\begin{aligned}\left\langle H_{\text{gyro}}\right\rangle &= M_0 J^2 + Q_{xx} J_x^2 + Q_{yy} J_y^2 + Q_{zz} J_z^2 \\ &\quad + D_x\,|S|\,\sigma_x J_x + D_y\,|S|\,\sigma_y J_y + D_z\,|S|\,\sigma_z J_z \\ &= \begin{pmatrix} h\,(J) + D_z\,|S|\,J_z & |S|\left(D_x J_x - \mathrm{i} D_y J_y\right) \\ |S|\left(D_x J_x + \mathrm{i} D_y J_y\right) & h\,(J) - D_z\,|S|\,J_z \end{pmatrix} \\ &= \begin{pmatrix} h\,(J) + d_z\cos\beta & \left(d_x\cos\gamma - \mathrm{i} d_y \sin\gamma\right) \\ & \quad \times \sin\beta \\ \left(d_x\cos\gamma + \mathrm{i} d_y \sin\gamma\right) & h\,(J) - d_z\cos\beta \\ \quad \times \sin\beta & \end{pmatrix}, \end{aligned} \tag{32.31b}$$

where

$$h\,(J) = M_0 J^2 + Q_{xx} J_x^2 + Q_{yy} J_y^2 + Q_{zz} J_z^2$$

and

$$d_\mu = D_\mu |S||J|\,. \tag{32.31c}$$

The dynamics generated by Hamiltonian approximations such as (32.31b) are analogous to other semiclassical approximations, such as the Maxwell–Bloch model of an atom in a cavity. Their solutions are very complicated and often chaotic. The classical variable ($\boldsymbol{J}$ in this case) follows phase contours on a changing RES that depends on the instantaneous expectation values of the quantum variables ($\boldsymbol{S}$ in this case), which in turn vary according to the instantaneous classical variables.

In spite of this complexity, semiclassical spectra may be approximated using RES pairs obtained from eigenvalues of a $2 \otimes 2$ matrix such as (32.31b) for each classical angular orientation ($\beta\gamma$) of the J-vector in the body frame [32.46, 47]. The results are pairs of surfaces roughly like those in Fig. 32.12a, but without the intersection lines. The Wigner non-crossing effect prevents degeneracy, except at isolated points.

Near-crossing RES are the rotational equivalent of near-crossing vibrational-potential energy surfaces (VES) described in treatments of *Jahn–Teller* effects [32.48, 49]. The classical, semiclassical, and quantum theory for such loosely-bound or fluxional systems is still inits infancy, but is potentially a very rich source of new effects.

References

32.1 G. Herzberg: *Molecular Spectra and Structure: Vol. I, Spectra of Diatomic Molecules* (Van-Norstrand-Reinhold, New York 1950)
32.2 G. Herzberg: *Molecular Spectra and Structure: Vol. II, Infrared and Raman Spectra of Polyatomic Molecules* (Van-Norstrand-Reinhold, New York 1945)
32.3 G. Herzberg: *Molecular Spectra and Structure: Vol. III, Electronic Structure of Polyatomic Molecules* (Van-Norstrand-Reinhold, New York 1966)
32.4 F. B. Wilson, V. C. Decius, P. C. Cross: *Molecular Vibrations* (McGraw Hill, New York 1955)
32.5 D. Papousek, M. R. Aliev: *Molecular Vibrational-Rotational Spectra, Studies Phys. Theor. Chem. 17* (Elsevier, Amsterdam 1982)
32.6 R. N. Zare: *Angular Momentum: Understanding Spatial Aspects in Chemistry and Physics* (Wiley Interscience, New York 1988)
32.7 W. G. Harter: *Principles of Symmetry, Dynamics, and Spectroscopy* (Wiley Interscience, New York 1993)
32.8 W. G. Harter, C. W. Patterson: J. Math. Phys. **20**, 1453 (1979)
32.9 W. G. Harter: Phys. Rev. A **24**, 192 (1981)
32.10 W. G. Harter, C. W. Patterson: J. Chem. Phys. **80**, 4241 (1984)
32.11 W. G. Harter: Comp. Phys. Rep. **8**, 319 (1988)
32.12 D. A. Sadovskii, B. I. Zhilinskii: Mol. Phys **65**, 109 (1988)
32.13 D. A. Sadovskii, B. I. Zhilinskii: Phys. Rev. A **47**, 2653 (1993)
32.14 I. M. Pavlichenkov: Phys. Rep. **226**, 173 (1993)
32.15 W. G. Harter, C. W. Patterson, F. J. daPaixao: Rev. Mod. Phys. **50**, 37 (1978)
32.16 W. G. Harter, C. W. Patterson: Phys. Rev. A **19**, 2277 (1979)
32.17 P. R. Bunker: *Molecular Symmetry and Spectroscopy* (Academic, New York 1979)
32.18 K. T. Hecht: J. Mol. Spectrosc. **5**, 355 (1960)
32.19 K. R. Lea, M. J. M. Leask, W. P. Wolf: J. Phys. Chem. Solids **23**, 1381 (1962)
32.20 A. J. Dorney, J. K. G. Watson: J. Mol. Spectrosc. **42**, 1 (1972)
32.21 K. Fox, H. W. Galbraith, B. J. Krohn, J. D. Louck: Phys. Rev. A **15**, 1363 (1977)
32.22 W. G. Harter, C. W. Patterson: J. Chem. Phys. **66**, 4872 (1977)

32.23 R. J. Butcher, Ch. Chardonnet, Ch. Bordé: Phys. Rev. Lett., **70**, 2698 (1993)
32.24 H. W. Kroto, J. R. Heath, S. C. O'Brian, R. F. Curl, R. E. Smalley: Nature **318**, 162 (1985)
32.25 W. Kratschmer, W. D. Lamb, K. Fostiropolous, D. R. Huffman: Nature **347**, 354 (1990)
32.26 O. Pfister: *Etude esperimentale et theorique des interactions hyperfines dans la bande de vibration ν_3 de la molecule* $^{28}SiF_4$ (Dissertation, Univ., Paris–Nord 1993)
32.27 J. Bordé, Ch. J. Bordé: Chem. Phys. **71**, 417 (1982)
32.28 Ch. Bordé, J. Bordé, Ch. Breant, Ch. Chardonnet, A. Vanlerberghe, Ch. Salomon: *Laser Spectroscopy VII* (Springer, Berlin, Heidelberg 1985) p. 95
32.29 W. G. Harter, D. E. Weeks: Chem. Phys. Lett. **132**, 187 (1986)
32.30 D. E. Weeks, W. G. Harter: Chem. Phys. Lett. **144**, 366 (1988)
32.31 D. E. Weeks, W. G. Harter: Chem. Phys. Lett. **176**, 209 (1991)
32.32 W. G. Harter, T. C. Reimer: Chem. Phys. Lett. **194**, 230 (1992)
32.33 W. R. Hamilton: Proc. R. Irish Acad. **II**, 424 (1844)
32.34 W. R. Hamilton: Phi. Mag. **25**, 489 (1844)
32.35 G. Stokes: Proc. R. Soc. London **11**, 547 (1862)
32.36 W. Pauli: Z. Phys. **37**, 601 (1927)
32.37 P. Jordan: Z. Phys. **94**, 531 (1935)
32.38 J. Schwinger: *Quantum Theory of Angular Momentum*, ed. by L. C. Biedenharn, H. van Dam (Academic, New York 1965) p. 229
32.39 L. C. Biedenharn, J. D. Louck: *Angular Momentum in Quantum Physics*, Encyclopedia of Mathematics, Vol 8, ed. by G. C. Rota (Addison Wesley, Reading, Massachusetts 1981) p. 212
32.40 I. I. Rabi, N. F. Ramsey, J. Schwinger: Rev. Mod. Phys. **26**, 167 (1954)
32.41 R. P. Feynman, F. I. Vernon, R. W. Helwarth: J. Appl. Phys. **28**, 49 (1957)
32.42 W. G. Harter, N. dos Santos: Am. J. Phys. **46**, 251 (1978)
32.43 K. K. Lehmann: J. Chem. Phys. **79**, 1098 (1983)
32.44 W. G. Harter: J. Chem. Phys. **85**, 5560 (1986)
32.45 Z. Li, L. Xiao, M. E. Kellman: J. Chem. Phys. **92**, 2251 (1990)
32.46 W. G. Harter: Comp. Phys. Rep. **8**, 319 (1988), see pp. 378–85
32.47 J. Ortigoso, I. Kleiner, J. T. Hougen: J. Chem. Phys. **110**, 11688 (1999)
32.48 H. A. Jahn, E. Teller: Proc. R. Soc. London **A161**, 220 (1937)
32.49 H. A. Jahn, E. Teller: Proc. R. Soc. London **A164**, 117 (1938)